
Article:
Chekotu, J.C. orcid.org/0000-0002-5304-0319, Goodall, R. orcid.org/0000-0003-0720-9694, Kinahan, D. et al. (1 more author) (2022) Control of Ni-Ti phase structure, solid-state transformation temperatures and enthalpies via control of L-PBF process parameters. Materials & Design, 218. 110715. ISSN 0264-1275

https://doi.org/10.1016/j.matdes.2022.110715

Materials & Design 218 (2022) 110715

Contents lists available at ScienceDirect

Materials & Design

journal homepage: www.elsevier.com/locate/matdes

Control of Ni-Ti phase structure, solid-state transformation temperatures and enthalpies via control of L-PBF process parameters

Josiah Cherian Chekotu [a,b,*], Russell Goodall [c], David Kinahan [a,b], Dermot Brabazon [a,b]

[a] Advanced Metallic Systems Centre for Doctoral Training, I-Form Advanced Manufacturing Research Centre, Dublin City University, Ireland
[b] Advanced Processing Technology Research Centre, School of Mechanical and Manufacturing Engineering, Dublin City University, Ireland
[c] Advanced Metallic Systems Centre for Doctoral Training, Department of Materials Science and Engineering, University of Sheffield, UK

HIGHLIGHTS

- Density of Ni-Ti controlled via control of L-PBF process parameters.
- Element concentration in Ni-Ti alloy controlled via L-PBF settings.
- Enthalpy and phase change temperatures controlled via L-PBF settings.
- Thermal variation in samples linked to resulting sample density.
- Thermal variation is samples controlled via alignment of print direction.

GRAPHICAL ABSTRACT

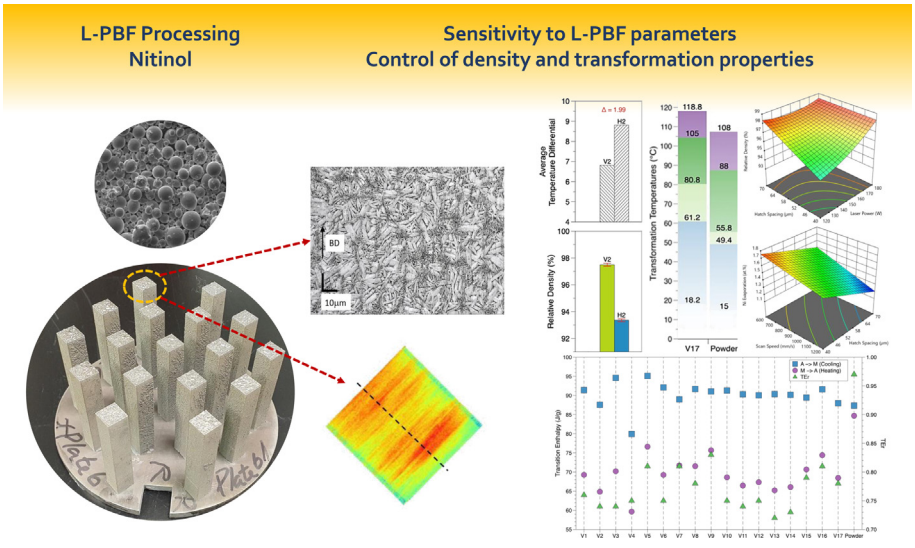

ARTICLE INFO

Article history:
Received 7 December 2021
Revised 20 April 2022
Accepted 30 April 2022
Available online 4 May 2022

Keywords:
Nitinol
Process optimisation
Laser powder bed fusion
Phase transformation
Shape memory effect
Differential Scanning Calorimetry (DSC)

ABSTRACT

In this work, nitinol samples were produced via Laser Powder Bed Fusion (L-PBF) in the horizontal and vertical orientations with systematic variations in laser power, scan speed and hatch spacing parameters. Increased density was positively correlated with increased laser power, scan speed and hatch spacing for the horizontally built samples but not for the vertically built samples. A smaller difference in the average temperature within a printed layer, associated with the vertically built samples, was linked with reduced porosity and reduced porosity variability between samples. Control of the L-PBF parameters was found to allow control of the resulting part chemical composition which also directly affected phase transformation temperatures, and related phase structures. The laser process parameters were found to have a significant effect ($p < 0.01$) on the martensite start/finish temperature, austenite start/finish temperatures, and the total temperature span. The volumetric energy density was also found to have a direct correlation with both the cooling ($r = 0.52$) and heating ($r = 0.53$) enthalpies, which was found to be due to increased

* Corresponding author at: Advanced Metallic Systems Centre for Doctoral Training, I-Form Advanced Manufacturing Research Centre, Dublin City University, Ireland.
E-mail address: josiah.chekotu2@mail.dcu.ie (J.C. Chekotu).

https://doi.org/10.1016/j.matdes.2022.110715

nickel evaporation. Such control of phase change properties afforded from L-PBF is important for many of the end applications for nitinol components including within the energy and precision actuation sectors.

1. Introduction

Unlike most polymeric and metallic shape memory materials, Ni-Ti or Nitinol intermetallic shape memory alloys (SMAs) have certain desirable mechanical and functional properties highly useful to the aerospace, smart structures, sensors/actuators, energy and biomedical sectors [1,2]. Ni-Ti is generally highly ductile, with low stiffness, good corrosion and wear resistances, and possess good biocompatibility. The composition of Ni:Ti is typically in a 50:50 ratio, however, based on applications, this can vary between 45:55 to 55:45 [1,3,4]. By controlling the composition, microstructure and processing conditions, Ni-Ti can be tailored with specific functional characteristics which can be exploited for bespoke applications. The various functional characteristics are shape memory effect, pseudoelasticity (mechanical phenomenon) and pseudoplasticity (thermal phenomenon).

The shape memory effect in Ni-Ti originates from the solid state phase transformations that occur during the deformation and/or thermal cycling [5]. When Ni-Ti with a martensitic phase is deformed, the crystal structure of the phase transforms to a detwinned martensite phase. When the temperature of the material is then raised above the transformation temperatures (TTs), the phase changes from martensite (B19′ monoclinic crystal structure) to austenite (B2 BCC structure) regaining the pretrained shape. When the material is then cooled to room temperature, the phase reverts back to a twinned martensite state. It has been found that a higher Ti content results in higher transformation temperatures enabling the shape memory effect to be set to that which is required depending on the application. A higher Ni content on the other hand can be set to lower the transformation temperatures sufficiently below room temperature such that the austenite phase is present and advantage can be taken of the superelastic (pseudoelastic) property of Ni-Ti, without the chance of phase change, for applications such as biomedical implants [2,5,6].

The superelasticity in Ni-Ti can recover from about 8–10% strain, before it deforms plastically. This remarkable property along with good damping curves, low stiffness, good corrosion resistance and good biocompatibility (TiO_2 prevents Ni leaching into the human body), enables Ni-Ti to be used in stents, implants, spinal fusion cage, bone plates/screws and other medical applications [7–12]. During phase transformations, latent heat is absorbed or released during the shape deformation or recovery. The solid-state phase transformations between martensite and austenite involve absorption/release of latent heat in a significant quantity [3,13,14]. This concept has inspired the use of Ni-Ti in heat pump and heat recovery applications, for which high heat transfer rates can be realised by creating Ni-Ti geometries with high surface areas.

Although Ni-Ti can be processed through several conventional manufacturing methods such as casting or powder metallurgy, the material is very difficult to fabricate in such processes, due to the high reactivity of titanium, and poor machinability of the alloy. Achieving a uniform and homogenous composition and producing complex structures using Ni-Ti are still challenges. With the advent of additive manufacturing (AM), the process of laser powder bed fusion (L-PBF) has been found to be highly compatible with Ni-Ti processing. Through this method, complex geometries can be created and the resulting part will require less or even no post-processing, and can have pre-designed porosity levels, homogeneous composition and tailored transformation properties [6,15–20]. The L-PBF method, also called selective laser melting (SLM), is widely used for fabricating metallic structures.

In L-PBF, initially a thin layer (<100 μm) of power is spread on a substrate plate placed on the build platform. A computer-controlled high-power laser beam is then scanned on the powder bed according to the 2D geometry slice extracted from the 3D CAD model of the part. The powder particles melt by absorbing the laser energy, and solidify to produce the shape specified by one cross-sectional slice (a layer) of the input CAD model. This step is repeated to build up the part layer-by-layer with the help of a spreader/recoater blade, an adjustable build platform and a powder delivery platform, until the complete 3D part is built. The laser process parameters such as laser power, scan speed, hatch spacing, and scanning strategy, control the intra/inter-layer thermal gradients and cooling rates which result in different microstructures leading to different part properties [15–17,21–23]. These complex thermal gradients and epitaxial solidifications can have a significant effect on the phase transformation characteristics of Ni-Ti. Over the past years, several researchers have worked on understanding the effect of L-PBF operational parameters on the part properties [21,24–28]. However, the investigation of the sensitivity of the functional characteristics of Ni-Ti to the material composition and L-PBF process control is still in its early stages and requires further research to provide sufficient fundamental understanding in these areas and subsequent end applications.

In this work, Ni-Ti bar-shaped samples were 3D printed using a L-PBF machine in both horizontal (bar long axis in the layer plane) and vertical (bar long axis normal to the layer plane) build orientations. The samples were then analysed for relative density levels, transformation temperatures, compositional changes, phases present, and thermal expansion properties. The primary aim was to investigate significant correlations of selected laser parameters with the chemical, thermal and physical properties of the L-PBF processed Ni-Ti. The results and findings enhance the existing fundamental knowledge and provide a better understanding of the design space for Ni-Ti.

There have been no studies to date which have examined the temperature evolution during the metal AM processing of Ni-Ti for measuring the effect of intralayer average temperature differentials on the resulting part densities. In addition, the effect of the process parameters on the Ni loss, phase transformation temperatures, the temperature range of each phase, and transition enthalpies and enthalpy ratios has not previously been presented. In this paper, the transformation characteristics and temperatures were measured via DSC and dilatometry thermal analyses. In this work, the significance of Ni reduction during the L-PBF process on the Ni-Ti thermal characteristics for the martensite, austenite and R-phases was also identified and elaborated. This paper fills these gaps in knowledge.

2. Methodology

2.1. Powder material

The Ni-Ti powders with a composition of Ni (49.9 at.%) - Ti (50.1 at.%) were supplied by Ingpuls GmbH, Germany. The higher Ti content was chosen in order to ensure that, after L-PBF, the shape

memory Ni-Ti phase change temperature was above room temperature. The composition was re-confirmed through an energy dispersive X-ray spectrometry (EDX) unit attached to a *Hitachi S5500* field emission scanning electron microscope (FE-SEM). To produce powders of suitable size and shape for L-PBF, the as-received powders were gas-atomised by electron induction melting inert gas atomisation (EIGA). The particle size distribution (PSD) was D_{10} = 12.3 μm; D_{50} = 28.1 μm; D_{90} = 57.3 μm, where D_{α} represents the diameter of the powder particles corresponding to the "α" volume percentage of particles present. The PSD was re-analysed using a *Malvern Mastersizer 3000* with an *Aero S* dispersion unit. The analysis was carried out using a refractive index of 1.958, and a particle absorption index of 1. The air pressure was set to 1 bar to prevent any particle aggregation and searing. Powder morphology was investigated using a *Zeiss EVO LS-15* SEM machine. The phase transformation temperatures of the as-received powders were also analysed, using a *Netzsch DSC 214* digital scanning calorimetry (DSC) following the ASTM F2004-17 standard, with liquid nitrogen for the sub-zero temperature range.

2.2. L-PBF process

Ni-Ti samples were 3D printed using the Aconity MINI (GmbH) SLM machine equipped with a Nd:YAG fibre laser system from IPG Photonics having a wavelength of 1068 nm, and a maximum power capacity of 200 W. The build chamber was installed with a rubber-based recoater blade. The chamber was flooded with argon gas (99.999% purity) to ensure minimum oxygen content (<50 ppm) throughout the printing process to reduce the chance of oxidation during melting and solidification. A powder supply factor of 1.8 (nearly twice the layer thickness) was used throughout the print to ensure a sufficient spreading of powder. In order to reduce spatter on fresh layers, the print sequence started from the inert gas exit side of the build chamber.

In order to reduce time, energy and material consumption, a Box-Behnken (BB) design of experiments (DoE) containing three factors (laser power, scan speed, hatch spacing) with three levels was followed, keeping layer thickness (40 μm) and spot sizes (50 μm) constant. The BB design includes sample production for repeatability analysis with the centre node repeated five times. Samples with these 17 sets of process conditions for each build orientation (Prefix: Horizontal – H; Vertical – V) were printed as shown in Fig. 1. The sample dimensions were 10 × 10 × 55 mm^3. Laser powers of 120, 150 and 180 W were used along with scan speeds of 600, 800 and 1200 mm/s, and hatch spacings of 40, 55 and 70 μm. The layer thickness of 40 μm was set based on the feedstock particle size distribution, to help ensure good powder spread and flowability on the build platform.

These parameter sets can be used to calculate the volumetric energy density, *VED*, which can be calculated as Eq. (1):

$$VED = \frac{P}{v \times h \times t} \tag{1}$$

where, P is the laser power (W); v is the scan speed (mm/s); h is the hatch spacing (μm); and t is the layer thickness (μm). The *VED* can be explained as the energy released from a unit volume of material during the L-PBF process. It can also be defined as quantifying the thermal energy readily available for the material to transit from powder state to a dense state [29]. For the current range of process parameters, the *VED* varies from 44.64 to 156.25 J/mm^3. Table 1 shows the complete set of process parameters in the DoE that were used to print the samples.

The samples were arranged on the substrate plate at an in-plane angle of 45° for vertical samples, and 30° for horizontal samples, in order to reduce any impact load on the recoater assembly, and to allow a more gradual gas flow/fume removal over the layers in the chamber during print. A simple stripe scanning strategy was maintained as shown in Fig. 2(a) with a rotation of 90° for each subsequent layer. This prevents any unwanted overheating around the corners of the sample. The build chamber ambient temperatures during the process were 20 ± 1 °C.

2.3. Sample characterisation methods

The densities of the as-fabricated H/V samples were measured by Archimedes principle following ASTM B962-17 with the help of an analytical balance, *Sartorius Entris II Essential BCE124I-1S*, having an accuracy and repeatability of ±0.1 mg. The samples were ground lightly to flat on all faces with 240 grit abrasive paper, and cleaned thoroughly. The weights of samples were measured in acetone, and densities were calculated. For the following characterisation methods, only vertically built samples were analysed, and no post-fabrication heat treatments were performed prior to analysis. The samples for different characterisation methods were extracted as shown in Fig. 2(b), these sub-parts were cut using diamond-infused blades with at constant slow traverse speed, to avoid excess heat or stress-induced microstructure alteration. DSC thermal analysis was performed on the 17 samples to obtain the heat flow properties and phase transformation temperatures. The thermal cycle range examined was from −60 °C to 130 °C, and then cooled back to −60 °C, maintaining a heat/cool ramp rate of 10 °C/min. The sub-zero temperatures were attained using liquid nitrogen. The same process cycle was followed for the powder

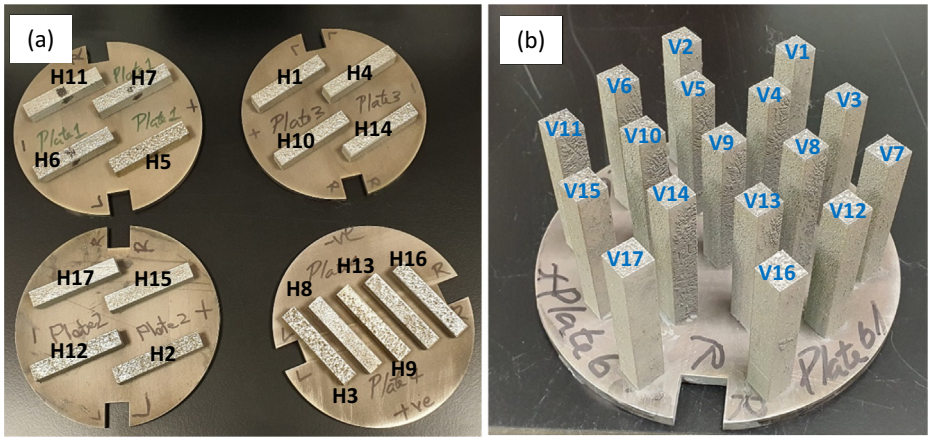

Fig. 1. Ni-Ti samples as printed on the Ni-Ti build plate - horizontally built samples (a); vertically built samples (b); prefix: V-vertical/H-horizontal.

Table 1
Laser process parameters used for printing the Ni-Ti samples.

Sample no. (V/H)	Laser power (W)	Scan speed (mm/s)	Hatch spacing (μm)	VED (J/mm^3)
1	150	900	55	75.76
2	120	600	55	90.91
3	180	600	55	136.36
4	180	1200	55	68.18
5	150	600	40	156.25
6	150	900	55	75.76
7	150	1200	40	78.13
8	180	900	70	71.43
9	180	900	40	125
10	150	900	55	75.76
11	150	1200	70	44.64
12	120	900	40	83.33
13	150	900	55	75.76
14	150	900	55	75.76
15	120	1200	55	45.45
16	150	600	70	89.29
17	120	900	70	47.62

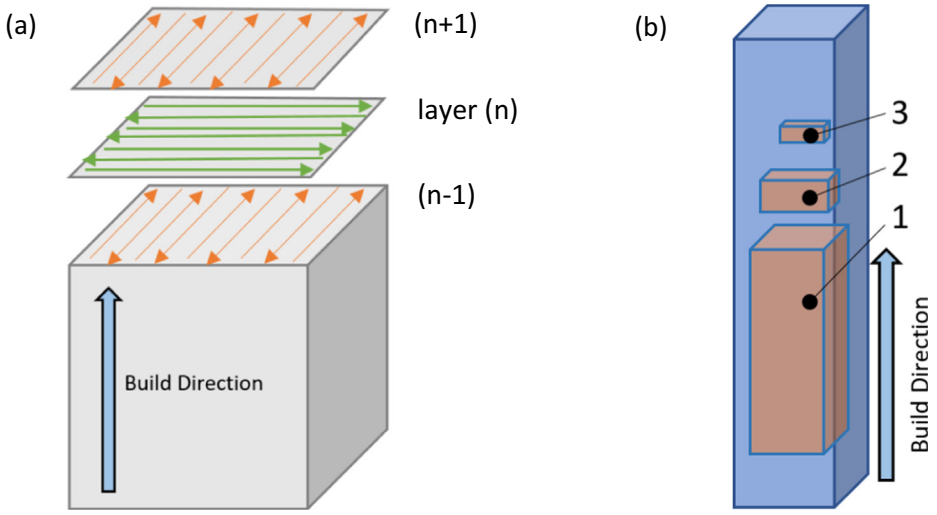

Fig. 2. (a) Scanning strategy illustrated showing the 90° rotation between each layer and scan direction reversal; (b) position of samples cut from the printed parts for various characterisations (1 - dilatometry; 2 - SEM/EDX; 3 - DSC).

samples as well. The L-PBF samples were prepared and tested adhering to the ASTM F2004-17 standard.

Dilatometry tests were conducted to identify the thermal expansion coefficients (CTE_S) and phase changes. For this, samples of dimensions 20x10x7.5 mm^3 were prepared with very flat, smooth and parallel surfaces for the dilatometry test which was conducted on *Netzsch DIL 402PC*. The samples were heated from room temperature to 250 °C and held for 10 min and then cooled back to room temperature. The heating/cooling rate was set to 1.5 °C/min. The correction samples, equipment calibration and sample preparation were based on ASTM E228-17 standard.

EDX was performed using the *Aztec Live System from Oxford Instruments NanoAnalysis* on *EVOLS15 version from Carl Zeiss* SEM machine, to identify the change in Ni content and investigate its effect on shape memory effect. The samples were cold-mounted and ground using SiC abrasive papers P240, 600, 800 and 1200, and then polished to a high surface finish using 6, 3, 1 μm diamond suspensions and 60 nm colloidal silica. Microstructure was revealed by swabbing with the etchant 15 mL HF + 10 mL HNO_3 + 10 mL CH_3COOH + 5 mL glycerol, for about 2–3 s. The above-mentioned SEM and an optical microscope *Keyence VHX2000E 3D Digital Microscope* were used to capture the microscopic images. X-ray diffraction (XRD) was used to analyse the phases present in the printed parts. A *Bruker D8 X-Ray Diffractometer* equipment with CuKα source having a wavelength of 1.5406 Å. The scans were performed in the 2θ range of 35° to 65° under locked coupled mode with an increment of 0.01° and 6.65 sec/step. The scan duration was 6 h for each sample.

2.4. Thermal data and response analysis

The thermal data of the melt pool was recorded by two pyrometers (from KLEIBER Infrared GmbH) setup in the Aconity SLM machine. The pyrometers detect the light emitted from the region of laser incidence (range of 1500–1700 nm), and the output infrared (IR) data is logged in terms of voltage (mV) units and coordinates on the build plate (x, y). In this work, single layer plot was made to illustrate the thermal gradients across the section of the sample. The data acquisition rate was 100,000 samples per second. A single build layer is represented by roughly 6 million data points, each containing the coordinate and temperatures (in mV). The temperature readings were translated to a normalised scale in a range of 0 to 1 to represent the thermal profile.

The output data (responses) from each of the experiments were analysed through Design-Expert 13 software, and only the models having a high significance and prediction reliability value with no

significant lack in data fit, are presented in the results section. The surface response equations are in terms of actual factors and the levels of each process parameters used. The equations also include coefficients appropriate to accommodate the actual units of each of the process parameters. The presented response surfaces each show the response to two of the input parameters with the third parameter kept constant at its mid-level.

3. Results and discussion

3.1. Particle analysis

The powders were found to contain a near-equiatomic composition of Ni (49.9 at.%) – Ti (50.1%) through EDX measurement. The particle size distribution shown in Fig. 3 is an average of three results obtained from the supplied material batch, and this is quantified using the parameter D_{α} which represents the diameter of the powder particles corresponding to the volume percentage (α = 10, 50 and 90) of particles present. D [4,3] is calculated by the equipment via the weighted average value by volume, and it can be considered as the average particle diameter, and does not depend on the number of particles. D_{10} = 12.3 ± 0.8 μm; D_{50} = 28.1 ± 2.2 μm; D_{90} = 57.3 ± 7.7 μm; D [4,3] = 34.0 ± 3.1 μm. The powders were observed to have near-spherical shapes as shown in Fig. 4. Most of them were almost perfect spheres, whereas some particles were ellipsoidal with tiny satellite particles (Fig. 4(b)) attached.

3.2. Input-output correlations

In order to check for possible correlations between the input process parameters and the responses, Pearson correlation and p-value significance parameters were used. Strong or relevant correlation was inferred for the responses that shows a Pearson coefficient (r) of 0.35 or greater, and a p-value of 0.05 or below in the model. A higher value of r and a lower p-value indicates a stronger correlation and a higher degree of significance, respectively. A negative r value indicates inverse relation, and vice versa. The term *VED* was not an input factor in the BB DoE model, and therefore the p-value is not applicable in the case of *VED*. All relevant correlations are listed in Table 2.

3.3. Density measurements

The densities of the samples were measured using Archimedes' method in acetone medium. The relative densities (with respect to theoretical density value of Ni-Ti = 6.45 g/cc) were found to vary between 97.2% and 97.9% for the vertically built samples, whereas

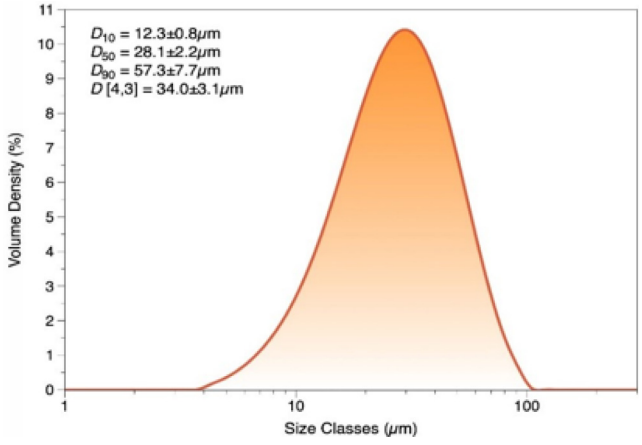

Fig. 3. Gaussian particle size distribution of raw Ni-Ti powders used.

for the horizontally built samples, larger variations between 93.4% and 98.5% were observed for similar process conditions. As seen in Fig. 5, most of the samples built in horizontal orientation showed lower densities compared to the vertically built samples. However, all of the samples (2,3,5,16) printed using the lower scan speed of 600 mm/s showed high reductions in densities. The other process settings for the horizontal produced samples (sets 4, 8, 9, 11 and 17) resulted in higher densities. These latter samples had a combination of higher laser power and lower energy density with large hatch spacing. It was also seen that for horizontal samples, the *VED* showed high negative correlation with the densities. The selected parameter levels did not cause a large variation in density the case of the vertically built samples.

For the relative density responses from 17 H/V samples printed with different laser powers (P), scan speeds (v) and hatch spacings (h), the actual equation for the relative density (RD) of printed samples, the response surface equations are reported as Eq. (2) and Eq. (3):

$$RD_{vertical}(\%) = 94.52953 + 0.032001P - 0.001192v + 0.051402h - (3.075E-06)Pv - 0.000572Ph + 0.000033vh \quad (2)$$

$$RD_{horizontal}(\%) = 63.82459 + 0.039849P + 0.035340v + 0.321426h - 0.000072Pv - 0.001757Ph + 0.000499P^2 - 0.000011v^2 \quad (3)$$

From these, it can be seen that for vertical samples that the laser parameters pose both linear and two-factor interactive effects on the relative density. In the case of horizontal samples, additional quadratic effects from laser power and scan speed are also observed. Fig. 6 shows the response surfaces of the effect of process parameters on vertical and horizontal builds; two process parameters are varied in each of the graphs while the third is kept at the medium levels. As seen in Fig. 6(a) and (b), the vertical build showed only slight variations (nearly planar effect) in densities with respect to the process parameters. From the model, it was found that only the interaction between laser power and hatch spacing showed a high level of significance (p = 0.0059) on *RD* for the vertical built samples. Larger variations along with quadratic response surfaces can be seen in the case of the horizontal builds (Fig. 6(c) and (d)). The scan speed showed the largest effect on the *RD* compared to laser power and hatch spacing. It was also found that for the current set of parameter levels, the *VED* has an inverse relationship with the resulting relative densities of the horizontally built samples.

In most of the earlier studies, more focus had been on understanding the effect of *VED* on the densification of Ni-Ti samples. However, depending on the parameter levels taken into account and factors that have been considered to remain constant, optimal *VED* values to obtain high *RD* varied widely between each of the studies. For instance, a high *RD* of 99% and above, were achieved by Saedi et al. [30] and Walker et al. [31] at a *VED* of 55 J/mm^3. Meier et al. [32] observed high *RD* at a *VED* of 85 J/mm^3. Haberland et al. [33] achieved an *RD* of 99% and higher, using a very high *VED* of 200 J/mm^3 whereas a *VED* of 111–126 J/mm^3 produced *RD* of >99% in work reported by Dadbakhsh et al. [34]. In the current study, the higher $RD_{horizontal}$ of 97.90% and 97.88% were attained using a *VED* of 125 J/mm^3 and 47.62 J/mm^3 respectively, and the high $RD_{vertical}$ of 98.31% and 98.52% were achieved for the same *VED* values respectively. All of these arguments including the results from the current work, point towards the requirement to use more detailed information than just the *VED* value for generating a correlation with the output RD. Such correlations could for example take into account in a more detailed manner the process

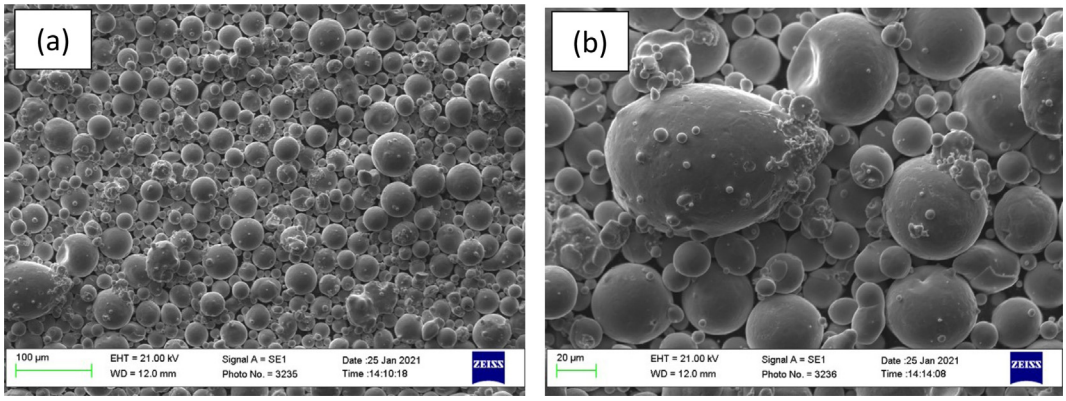

Fig. 4. Powder morphology as observed in SEM (secondary electron): spherical (a) and magnified view of an ellipsoidal particle (b) with some attached satellite particles.

Table 2
Pearson coefficients and p-values indicating input-output correlations.

Correlation	r	p
Vertical Samples		
Laser Power –*Ms*	0.4063	0.0009
Scan Speed –*Ms*	−0.5000	0.0009
Hatch Spacing –*Ms*	−0.6563	<0.0001
Laser Power –*Af*	−0.7855	<0.0001
Laser Power –*RMTR*	−0.5238	0.0123
Hatch Spacing –*RMTR*	0.5139	0.0136
Laser Power –*TTR*	−0.6463	0.0007
Scan Speed –*TTR*	0.5122	0.0039
Scan Speed – Ni Evaporation	−0.5817	<0.0001
Hatch Spacing – Ni Evaporation	−0.6980	<0.0001
VED– Ni Evaporation	0.8585	N/A
VED– Endothermic Enthalpy	0.5333	N/A
VED– Exothermic Enthalpy	0.5155	N/A
Horizontal Samples		
Laser Power – Density	0.4122	0.0001
VED– Density	−0.4825	N/A
Scan Speed – Density	0.5847	<0.0001
Hatch Spacing – Density	0.4207	0.0001

parameters and potentially also other properties such as the powder and inert gas related properties.

The *RD* variations in both H/V samples can be understood in relation with the thermographs plotted in Fig. 7. The figures show the normalised thermal profiles of the middle layer for one plate of the horizontal builds and one of the vertical build. It can be seen that the horizontal samples underwent large thermal variations in the samples across the build plate as compared to the vertical samples with the same process conditions. As seen in Table 2, it can be seen that the effect of energy density was substantial in the case of horizontal samples. For instance, sample H15 (VED = 45.45 J/mm^3) has the least variable overall temperature profile, whereas H17 with 47.62 J/mm^3 has a slightly higher variation in thermal profile. Sample H12 with 83.33 J/mm^3 and H2 with 90.91 J/mm^3 exhibited the highest variation in temperature profile. This logically follows from the processing conditions, as the horizontal build has a larger surface area and therefore a larger time interval between the print of each layer. This leads to higher extent of heat dissipation increasing the temperature differential across the layer and also would produce larger interlayer thermal gradients when compared to the vertical builds. In the vertical samples,

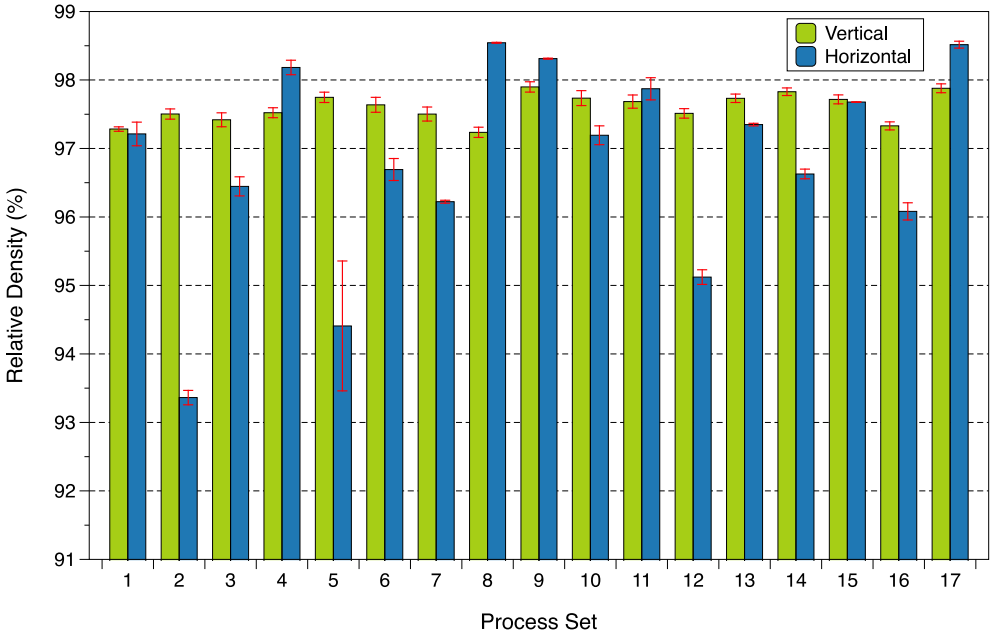

Fig. 5. Relative densities of samples built vertically and horizontally using the set of 17 process conditions, measured using Archimedes principle; 95% confidence interval implemented based on n = 3.

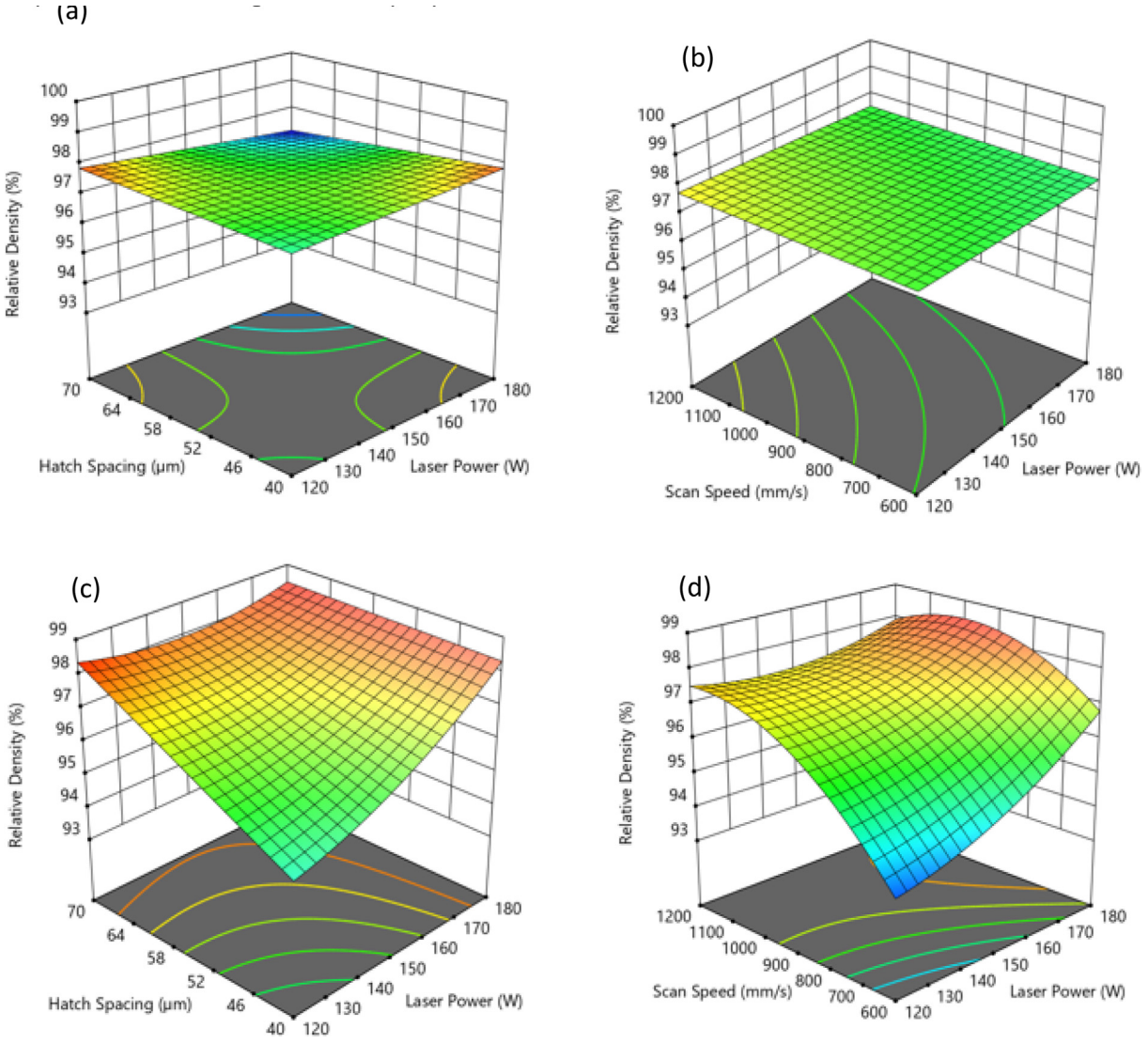

Fig. 6. Response surfaces showing the effects of the laser process parameters on relative densities of the vertically built samples (a) with v = 900 mm/s and (b)h = 55 µm; and on the horizontally built samples (c) with v = 900 mm/s and (d) h = 55 µm.

the temperature differential is lower (sample V2; more uniform colour map in Fig. 7 (b)) than is evident from the horizontal sample colour maps (Fig. 7 (a)), where the rate of change of the temperature gradient from one end of the sample to the other appears to be higher.

The average temperature differentials (TD_{avg}) of each of the samples on the horizontal build shown in Fig. 7, were also compared to those recorded from the samples printed in the vertical orientation. The average differentials were calculated using the normalized temperature data through the centerline as shown in the enlarged color maps of H2 and V2 in Fig. 7. TD_{avg} was calculated by first obtaining the rolling differential of the consecutive data points and then averaging the sum of the differentials. Even though the TD_{avg} did not show a significant correlation with the actual density values, it indicated a noticeable trend with how density varies. As shown in Fig. 8, it can be seen that the densities are typically higher when the TD_{avg} is lower, and vice versa. The differences in the TD_{avg} of vertical and horizontal samples are indicated by Δ. As Δ decreases, the difference in densities were also found to decrease. In the case of samples H/V 17, the Δ was negative, and this reflected as density being higher for H17 compared to V17. In general, the vertical samples were found to have a lower TD_{avg}, indicating a more uniform intra-layer thermal profile which then translated into smaller density variations and a less significant direct and two-factor interaction relation. In contrast, the higher TD_{avg} in the horizontal samples can be seen to have resulted in larger variations in density within the horizontal samples, for similar parameter sets. This is also supported by the statistical data shown in Table 2.

These larger temperature differentials and interlayer thermal gradients extend to causing various defects in the samples, and are found here to have resulted in lower sample densities. In addition to the density results, this is corroborated by the optical micrographs shown in Fig. 9 (c and d), where porous defects are found to be significantly high in sample H2 compared to sample V2. After the density tests, wire-EDM was performed on sample H2, and sample V2 is in the same condition (240 grit finish) as used for density tests. These different surface finishes can be ignored at the moment to focus attention on the presence of pores.

The porosities found in L-PBF processed parts can be identified based on the causes of occurrence and morphologies. Sufficient laser power and *VED* is necessary to melt the powder on one layer

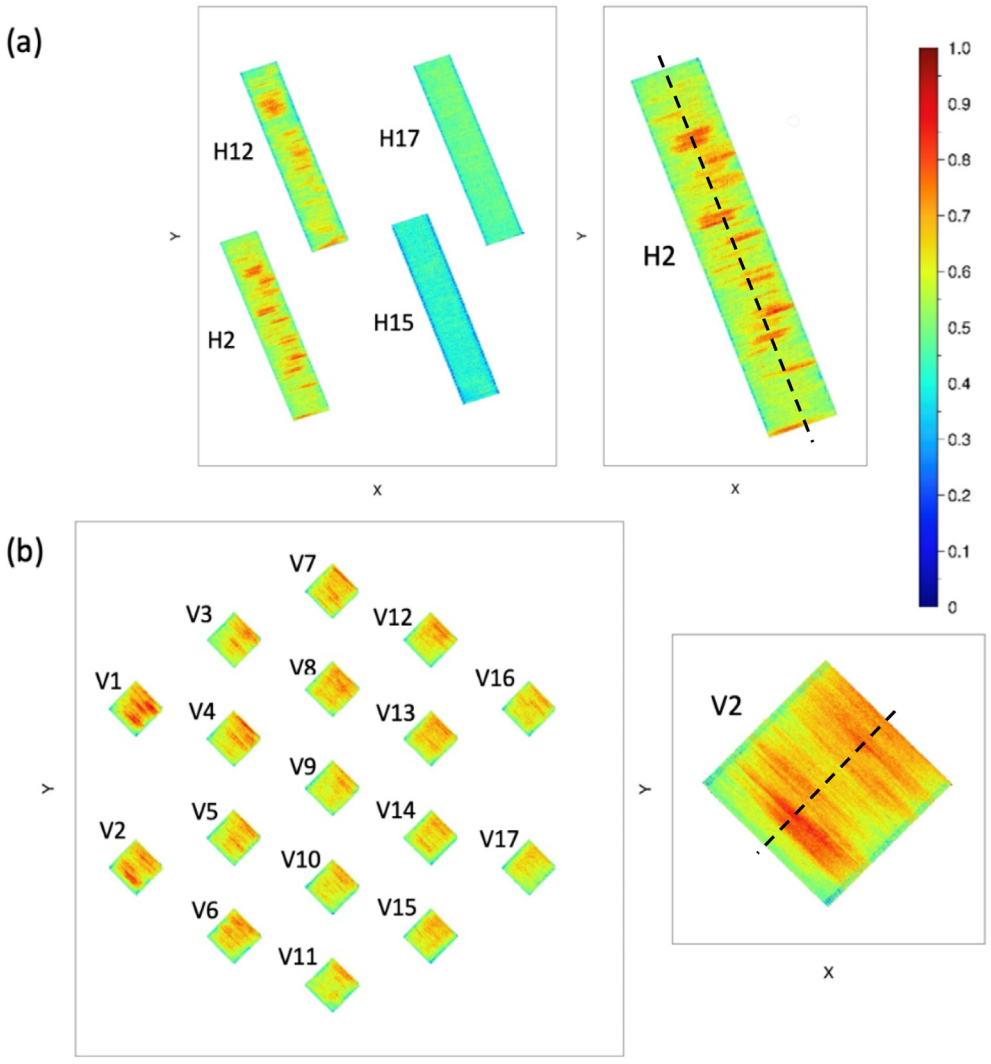

Fig. 7. Thermal IR data plots showing the temperature variations across the middle layer in: (a) horizontal build including the magnified view of samples H2, and (b) vertical build including the magnified view of sample V2; normalized temperature scale has been used.

and re-melt the previous layer, to ensure epitaxial solidification. This is necessary for strong interlayer bonding which helps to prevent undesirable intermetallic phases, and various types of pore formations [5]. Almost all of the samples were found to contain a set of irregular pores or voids. These occur due to various process-induced effects. One of them is the balling defect which occurs due to the expansion of trapped oxygen between layers producing a collapsed region or retention of the pore. Epitaxial solidification and low oxygen levels are necessary to reduce the chances of these irregular pores. The partial pressure at equilibrium for oxygen (near the melting point of Ti) has to be less than 16.2 bar to avoid oxidation. This is generally very impractical, and therefore, oxidation cannot be completely ruled out in L-PBF processes even though the chamber is flooded with argon or other inert gases [34,35]. Irregular pores can also be formed due to lack of fusion. These are found in larger sizes (few hundreds of microns), and is commonly seen spanning along the boundaries of several melt pools. As seen in Fig. 9(a), these defects in some cases accompany unmelted powder particles. This indicates the lack of fusion due to insufficient laser energy which fails to generate an effective melting and region of fusion overlap.

Many of the porosities found near the edges of the vertically printed samples (sample V2 presented in Fig. 10) were of gas-induced type. These pores are spherical in shape and occur due to the trapping of ambient gas in the powder bed; not having sufficient time to escape the melt pool. Since a huge fraction of spherical pores were formed near the edge regions, this can be also due to a coupled effect of process conditions (e.g., high scan speed) that could have resulted in poor gas removal and insufficient melting near the edges. The observed sizes of these pores were in the range of 5–50 μm. The formation of gas induced pores is a dynamic process that involves nucleation and growth of pores, and then an eventual out-gassing (removal/escape of gas) during the rapid solidification of melt pools. Due to insolubility of these gases in liquid metals, the gas pores follow Marangoni convection to escape easily through the melt pool surface. High energy densities tend to generate high temperatures which might evaporate lower melting point constituents (for instance, Ni) accelerating the pore nucleation. At the same time, a higher energy density can induce a higher thermal gradient between the apex and boundary of the melt pool, which in turn boosts the Marangoni convection accelerating the out-gassing process [36,37].

Along with the above-mentioned porosities, some large voids were also observed in samples H2 and V2. These are also a few hundreds of microns in size and more of an irregular spherical morphology. These can be identified as the keyhole porosities. The keyhole pores are caused under high instability in the melt pool due to surface tensions and hydrostatic pressures generated

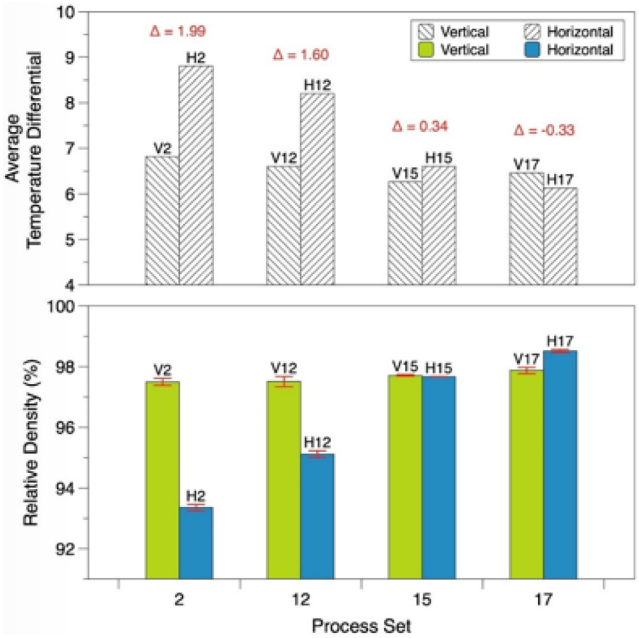

Fig. 8. Average temperature differential for vertical and horizontal samples 2, 12, 15 and 17, difference in differentials of vertical and horizontal samples of each set are denoted by Δ.

by the high energy density or localized high penetration of laser beam [38]. These are often formed near the bottom region of the melt pool and can be seen in BD view (Fig. 9(c)) of sample H2. The formation regions can be somewhat assumed to be melt pool boundaries. It is to be noted that the spot size (50 μm) and hatch spacing (40, 55, 70 μm) in the current work causes laser tracks to overlap to a higher extent than in many previously published works. This can create localized thermal instabilities that could favor the keyhole formation.

The porosity in particles is formed during the gas atomization process, and imperfections such as satellites and skewed sphericity as seen in Fig. 4 can also lead to porosity. This causes inhomogeneity during powder deposition and could result in air pockets between the thin layers. Another possible cause of porosity is the presence of spatter/melted droplets from the melt pool produced during the previous scans. As explained by researchers [25,36,39–41], this might occur at higher *VED* values and lower scan speeds, causing the pressure in the melt pool to exceed the surface tension levels of the molten material.

The L-PBF process tends to create residual thermal (unbalanced) stress profiles between the printed layers. These stresses are usually caused by the large thermal gradients from multiple remelting and solidification cycles. The thermal expansion on one layer creates tensile stress while the layer beneath undergoes compressive stresses. This differential stress phenomenon is induced across the underlying layers, and these layers can be affected in this way multiple times. This can ultimately lead to delamination or warpage of samples from the build plate. As scan overlaps are highly possible with the laser process parameters used in this work, the possibilities of residual stresses are quite high. This can initiate cracks throughout the cross-section of the layer affecting the mechanical properties. The presence of microcracks can be seen in Fig. 9(b). These effects can create pores which could act as crack nucleation sites and end up in crack propagation. However, the rapid cooling in L-PBF can suppress the propagation mechanism in the structure [42,43] and result in shorter microcracks.

Observing the microscopic view of sample cross-section in Fig. 10(c), we can see a rectangular pattern. This pattern can be confirmed as a forefront of the brick-like structures that extend beneath the surface, as seen through a fractured face (Fig. 10(d)) of the same sample. At the molecular scale, Ni-Ti is extraordinarily ordered as compared to most of the metals/alloys that form random solid solutions, rather than an orderly arrangement as seen inside a diamond or salt crystal. However, the Ni-Ti structure is arranged in cubic form with almost 90°angles resulting in these brick-like structures. The right angle arrangement becomes acute or obtuse under the application of heat, and the shape is deformed. Upon cooling, the structure again becomes cubic and regains the right angles and the original programed shape is regained (shape memory).

3.4. Transformation temperatures

The transformation temperatures were calculated from the heat flow vs temperature graphs generated through the DSC analysis as shown in Fig. 11. Each peak starting and ending from the baseline represent the presence of a stable phase. The stable phases found were martensite (low temperature phase with monoclinic B19′ crystal structure) and austenite (high temperature phase with body-centred cubic B2 crystal structure). The start and finish temperatures of each of these phases are estimated by plotting tangent lines where the heat flow deviates from the baselines, as illustrated in Fig. 11.

Compared to the raw powders, most of the as-fabricated samples exhibited an overlapping peak merged with the austenitic transformation region. Due to this, the peaks may appear slightly wider in L-PBF samples. In the raw powders, a shoulder can be seen on either peaks denoting an inhomogeneous heat flow among the powder particles [44]. This indicates the presence of a third unstable intermediary phase; identified as an unstable variant (R^*) of the R-phase (rhombohedral crystal structure). The R^* formation is mainly caused by the cold work performed during the fabrication. This can be further accelerated if Ni-rich precipitates are present [5,45]. A shift of the peaks to the higher side of TTs was observed, see Fig. 12 (a). The critical transformation temperatures considered are martensite start (*Ms*) and finish (*Mf*) temperatures, R-phase variant start (Rs^*) and finish (Rf^*) temperatures, and austenite start (As) and finish (*Af*) temperatures. Since all of the samples containing R^* phase has an overlapping peak, Rf^* and *As* can be considered as the same point.

The transformation temperatures were found to be highly sensitive to the Ni-Ti composition as shown in Fig. 12, which represents the experimental results from several research works in the past [46]. In the L-PBF process, the high laser energy results in faster evaporation of Ni due to its lower melting point (1455 °C) as compared to that of Ti (1668 °C). Another possibility of this compositional change owes to the formation of stable phases such as Ni_3-Ti or Ni-rich precipitates such as Ni_4Ti_3 (metastable) which ultimately depletes the Ni content in the matrix giving rise to TTs due to the remaining higher Ti content. However, these phases or precipitates generally do not affect the shape memory effect (SME) directly, instead it changes the composition of the matrix [5]. At times, the distribution of Ni and Ti could be non-uniform in indicated by a number of additional small peaks in DSC curves which can adversely affect the shape recovery [47].

All of the current samples in the as-fabricated state exhibited a Ni reduction of 1.2 to 1.8 at.%. The *Ms* for raw powder (Ni – 49.9 at. %) was found to be 49.4 °C which agrees with the literature values seen in Fig. 12. The Ni reduction that occurred in the current study was found to elevate the transformation temperatures in general compared to the raw powders (Fig. 13). Since the current feedstock has a higher Ti content, the rise in transformation temperatures are not considerably high, as compared to that of the samples printed using Ni-rich Ni-Ti powders [46,48]. The increased *Ms* tempera-

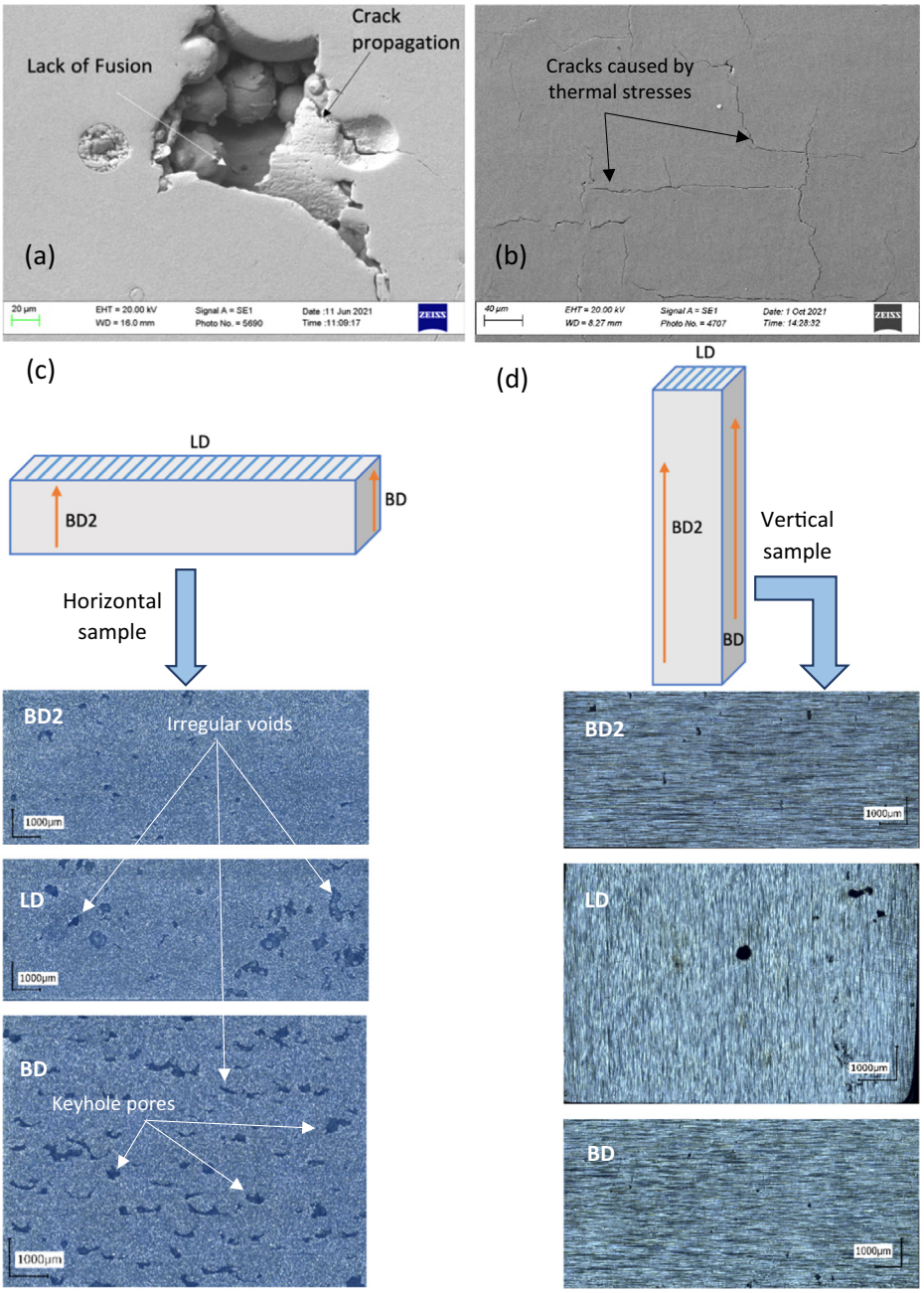

Fig. 9. (a) SEM image showing porosity found in sample V11 showing lack of fusion indicated by unmelted particles trapped between layers; (b) microcracks of sample V7; optical micrographs showing the extent of porosities observed on (c) horizontally built (H2) and (d) vertically built (V2) samples having same process parameters. (LD – sectional lateral face corresponding to print layer; BD and BD2 – faces corresponding to the build direction as illustrated).

tures of L-PBF processed samples were found to have very small variations between 61.2 °C and 63.3 °C. This further agrees with the literature findings for corresponding Ni contents (48.1 to 48.7 at.%); the *Ms* temperatures become steady around 60 to 65 °C for this compositional range. Further to the L-PBF process, the *Mf* temperatures increased by 1.2 to 9.0 °C, and *Ms* temperatures increased by 11.8 to 13.9 °C. The *Rs** increased by 20 to 25 °C, and *Rf** or *As* increased by 7.0 to 19.8 °C, while *Af* increased by 5.0 to 13.9 °C. It can be also seen that the martensite transition and R-phase transition temperature span increased in the L-PBF samples as compared to that of the raw powder used.

An XRD analysis was performed at room temperature (20 °C) on two L-PBF samples and raw powder to identify the different phases present. As observed in Fig. 14(a), the patterns confirm the presence of mostly B19′ martensite phases. The presence of martensite phase in the matrix was also confirmed in microscopy, seen in the form of needle-like structure (Fig. 14(b)). The peak around 60° indicating an R (2 2 2) phase or a B19′ (1 2 1) was stronger for the raw powders. The peak around 41° showing B19′ ($1\ \bar{1}\ 1$), was weaker in the case of V7, however, it was stronger and wider in the case of V2. Comparatively, most of the B19′ peaks were stronger and wider in the case of V2. Some of the minor obscure peaks may indicate the presence of secondary phases such as $NiTi_2$ and Ni_3Ti [49]. The presence of R-phases and precipitates or secondary phases might be caused due to intense thermal stresses generated from the processing conditions. The presence of Ni_4Ti_3 precipitates often results in a stable R-phase [49].

It has to be noted that the austenitic transformation (heating cycle) is an endothermic process, while the martensitic transforma-

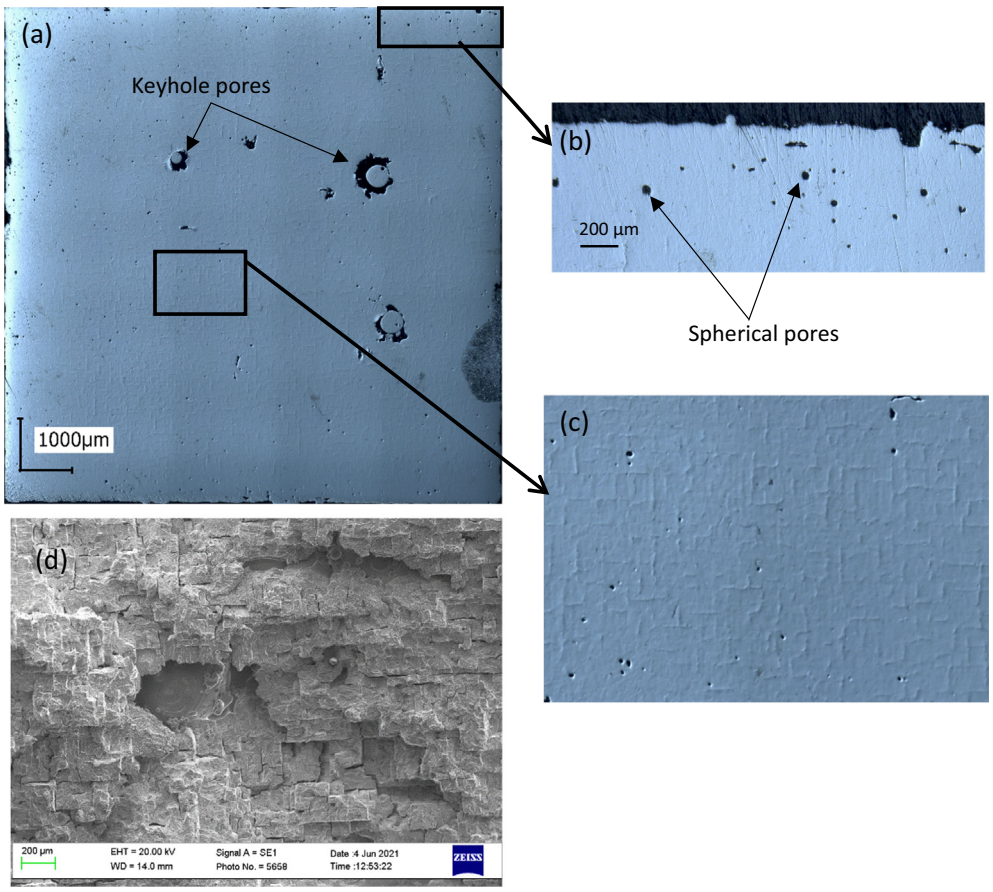

Fig. 10. (a) Polished LD face of sample V2 showing the presence of keyhole pores; (b) detailed view of spherical gas-induced pores formed along the edges; (c) magnified view showing the rectangular patterns; (d) fractograph showing brick-like structures beneath the rectangular pattern on the surface.

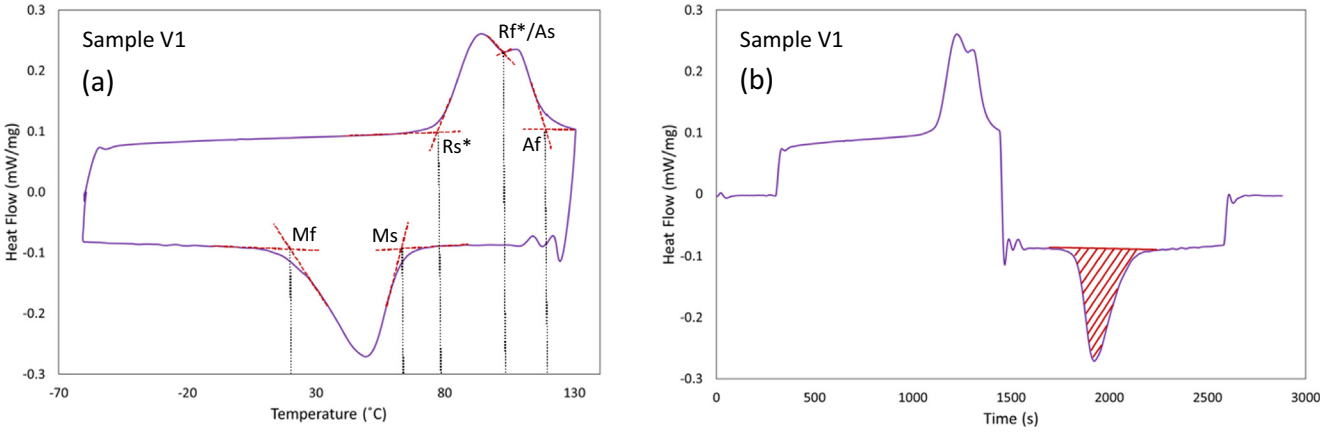

Fig. 11. Illustration of determining the (a) transformation temperatures and (b) transition enthalpy from the DSC graphs.

tion (cooling cycle) is an exothermic process involving enthalpy changes. This transition enthalpy (J/g) was determined by plotting the heat flow curve (W/g) generated via DSC against the time parameter (seconds). The martensitic transformation peak in the new plot (Fig. 11) is then isolated, and the area enclosed by the peak is calculated by integrating the curve using MATLAB trapezoidal numerical integration (*trapz*) function to get the cooling enthalpy ($\Delta H_{cooling}$). A similar method is followed for the austenitic transformation peak to get the heating enthalpy ($\Delta H_{heating}$). As observed in Fig. 15, the transition enthalpy changes during the heating and cooling cycles are different from each other. In general, the enthalpy change during cooling cycles is higher compared to that of the heating cycles. To better understand this calorific difference, the transition enthalpy ratio (*TEr*) was calculated using Eq. (4).

$$TEr = \frac{\Delta H_{heating}}{\Delta H_{cooling}} \tag{4}$$

Referring to Fig. 15, it can be seen that after the L-PBF processing, the *TEr* values dropped from 0.97 (raw powder) to a range of 0.72–0.83. Ideally, the net heat inflow or outflow should be equal and balanced (*TEr* = 1), indicating complete phase transformation of the material. However, due to the processing conditions, mate-

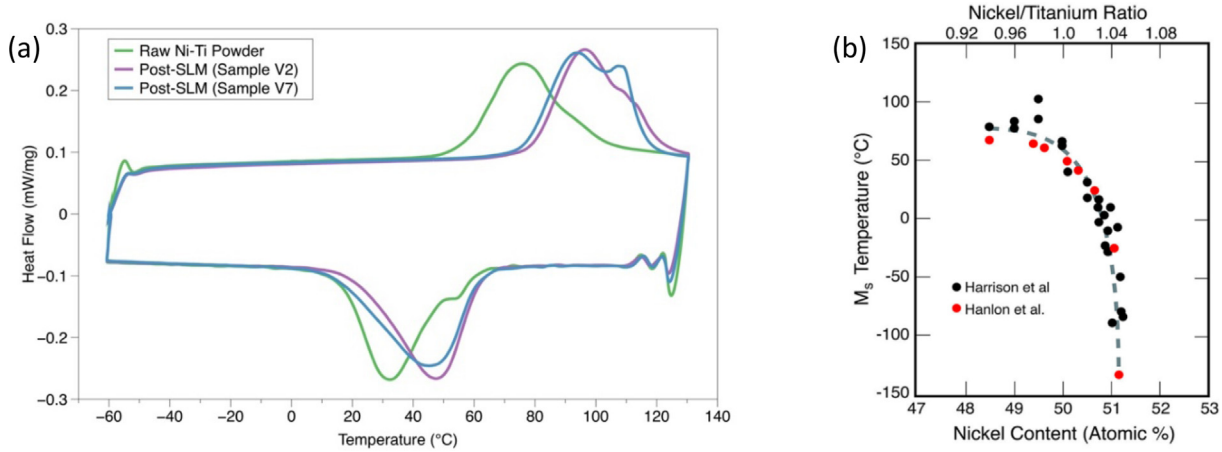

Fig. 12. DSC plots showing the shift in transformation peaks and the presence of an intermediate phase after L-PBF processing compared to the raw powders (a); variation of martensite start temperature (Ms) with Ni content (b) [46].

Fig. 13. Ni evaporation (increase in Ti content) in all samples and their transformation temperatures showing different phases: Austenite transition (Af-As); R-phase transition stage 1 (As-Rs*); R-phase transition stage 2 (Rs*-Ms); and Martensite transition (Ms-Mf).

rial inhomogeneity and different entropies in play, the extent of transformation can differ in a real scenario. The entropies are linked to the thermal and dynamic equilibrium, and the entropy production due to phase transformations [50]. This results in a difference in calorific values during heating and cooling cycles. It is interesting to note that the raw powder has a high *TEr* value close to 1; indicating a good compositional homogeneity and least thermal or dynamic entropies. As mentioned earlier, the *TEr* value can also point towards the extent or volume of material undergoing phase change. Based on the $\Delta H_{heating}$ and $\Delta H_{heating}$, it can be implied that the material transformed to austenite (heating) decreased by 10–30%, while the transformation to martensite (cooling) increased by 1–9% in the case of L-PBF samples (Fig. 15). It is interesting to note that *VED* showed a high positive correlation with the cooling (r = 0.5155) and heating (r = 0.5333) enthalpies, which also positively correlated with a relative increase in Ti content within the alloy.

Analysing the effect of the laser process parameters on TTs, it can be seen that certain critical temperatures or range of temperatures showed a significant effect on these values. Martensite start temperatures generally lie about halfway across the transition temperatures span, and therefore they can be used as a quick reference to understand the functional property that the material might possess. The full transformation temperature range, *TTR* = *Af* − *Mf*, and *Af* temperatures indicate the boundaries of a transition span. This could help the engineers to identify the operational range of the material for specific applications. $Rs^* \rightarrow Ms$ transformation range (*RMTR*) is the transition span where the phases are unstable as the crystal structure tends to change dynamically to the most suitable variant of martensite or R-phase or austenite. In the current DoE, *Ms* was found to have a linear relation (Eq. (5)) with the process parameters (Fig. 16(a) and (b)); scan speed and hatch spacing poses an indirect relation with higher significance, while the laser power poses a direct impact on *Ms*. *Af* was

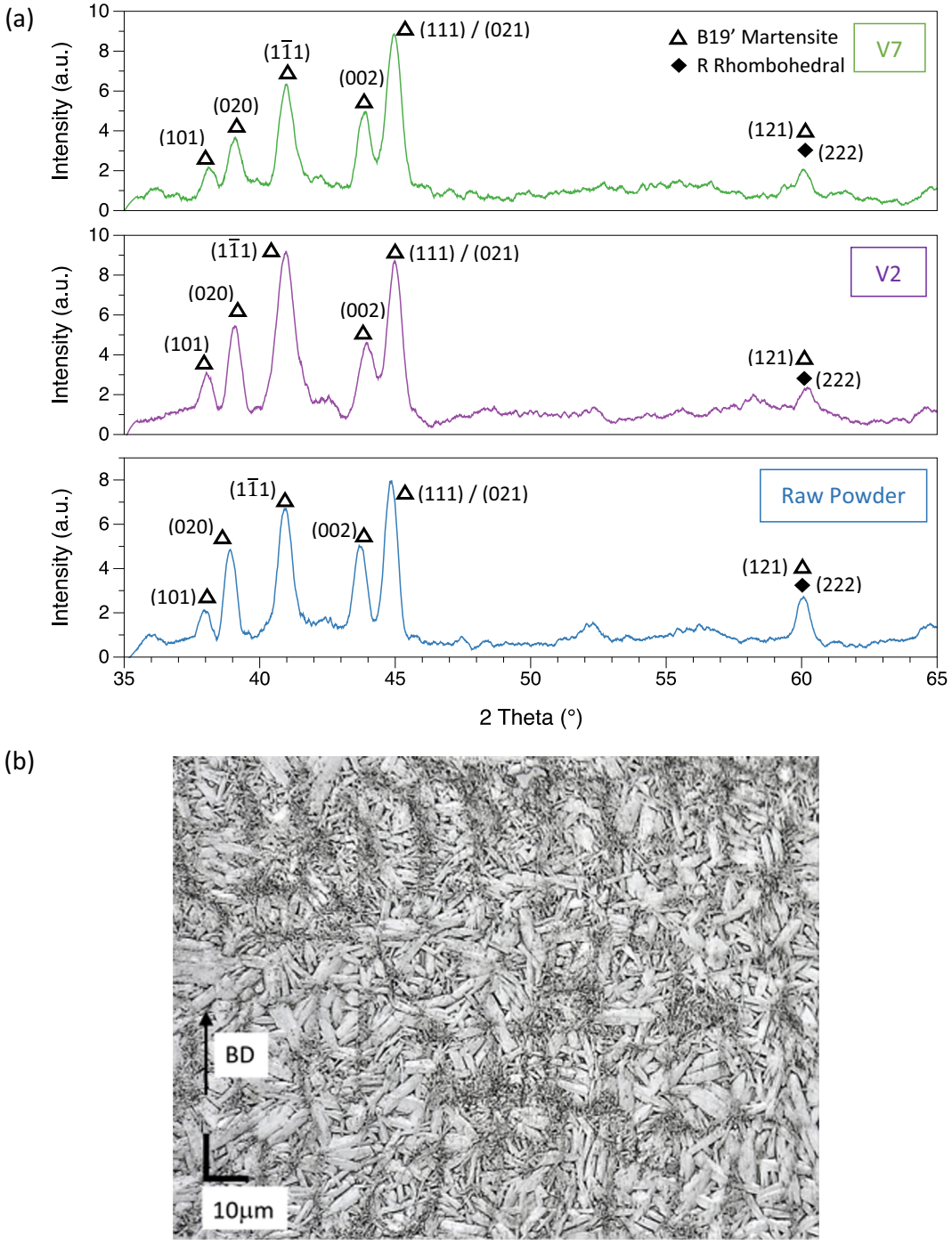

Fig. 14. (a) X-ray diffraction patterns observed in raw powder, and the L-PBF produced samples V2 and V7; (b) martensitic structures as seen in optical micrograph of sample V2.

found to have a two-factor interactive (Eq. (6)) relation (Fig. 16(c) and (d)); however, laser power exhibited a stronger indirect influence on the *Af* compared to the other two parameters. A linear relation (Eq. (7)) was found to exist with the *RMTR* range also. Laser power exhibited an indirect relation with a higher significance, while a direct effect on *RMTR* was observed with the hatch spacings (Fig. 16(e)). In a recent work by Zhu et al [48], hatch spacing was found to have a linear relation with TTs, which may be attributed to a reduction in Ni content and increasing dislocation densities. In the case of *TTR*, the estimated relation (Eq. (8)) was again found to be linear, having the laser power posing a negative relation with high significance, and the scan speed posed a positive relation. The response surface for *TTR* is shown in Fig. 16(e).

$$Ms(C) = 63.68235 + 0.012083P - 0.001208v - 0.035h \quad (5)$$

$$Af(C) = 168.55294 - 0.382222P - 0.009056v - 0.45h + 0.000094Pv + 0.003889Ph - 0.000111vh \quad (6)$$

$$RMTR(C) = 15.85245 - 0.044167P + 0.001667v + 0.086667h \quad (7)$$

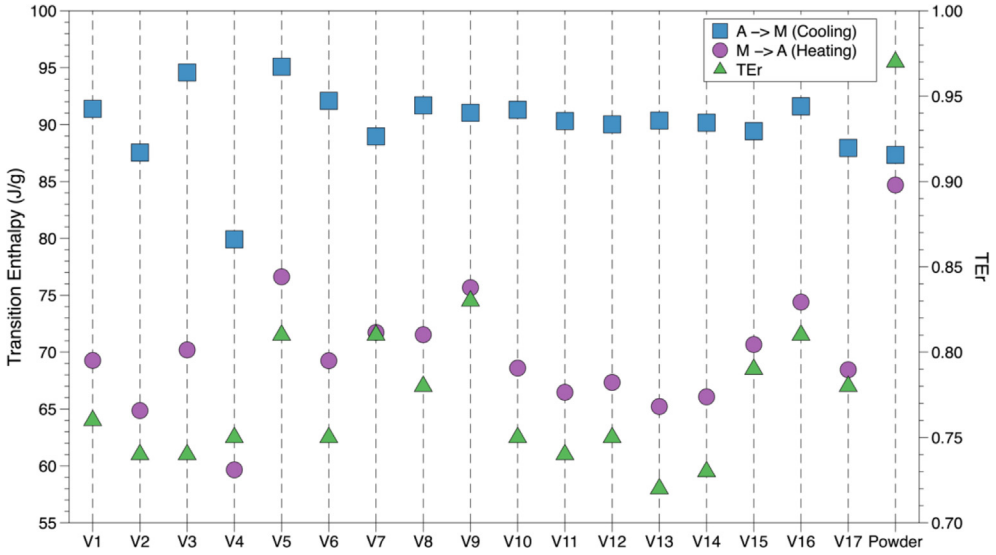

Fig. 15. Enthalpy changes during austenitic and martensitic transformations, and enthalpy ratio (TEr) for each of the L-PBF samples and raw powder.

$$TTR(C) = 100.94608 - 0.100417P + 0.007958v + 0.063333h \quad (8)$$

3.5. Nickel evaporation

As discussed in the previous section, Ni evaporation or increase in Ti content in the matrix have a significant effect on the shape memory behaviour of the material by increasing the TTs. In the current work, the raw powder had Ni composition of 49.9 at.% which is just around the corner of the plateau region in the graph shown in Fig. 12. Therefore, the change in Ni content (1.2–1.8 at.%) that occurred in the L-PBF resultant samples did not cause a huge change in the TTs. If the Ni content had been higher in the raw material, the effect of Ni evaporation would have been considerable. Thus, the level of Ni evaporation plays a critical role in determining the performance of the functional property for the specific application. It is necessary to have high input energy to cause this phenomenon, and therefore the effect of laser process parameters needs to be addressed.

From the response analysis, it can be seen that a two-factor interactive relation (Eq. (9)) exists between the Ni evaporation and process parameters in the current DoE. Fig. 17 shows the response surfaces representing the combined effect of process parameters on Ni evaporation. It was found that the scan speed and hatch spacing (with higher significance) posed a negative relation with the output. It was also seen that the *VED* shows a highly significant (>85%) direct relation with the Ni evaporation. A narrower hatch spacing causes laser track overlap which ultimately results in high *VED*, and this finding correlates well.

$$\begin{aligned} Ni_{evaporation}(at.\%) = {} & 0.905882 + 0.008333x - 0.000528y \\ & + 0.02z + (2.77778E-06)xy \\ & - 0.000167xz - (5.55556E-06)yz \end{aligned} \quad (9)$$

3.6. Thermal expansion characteristics

The linear thermal expansion properties of all L-PBF samples were analysed through dilatometry. Thermal strain curves were formulated as shown in Fig. 18 (a), based on the thermo-mechanical data generated by the instrument. The linear thermal expansion coefficients (CTE_S) were then calculated (Eq. (10)) by taking the slopes of the thermal strain curves around a selected region where the linear expansion is stabilised or where a steady state of stable phase is found. The heating and cooling cycles exhibited slightly different slopes, and therefore an average of these values were used to quantify the resultant CTE values used for the study.

$$CTE = \frac{\Delta L}{L_0.\Delta T} \quad (10)$$

where, ΔL denotes the change in one linear dimension, L_0 is the original length, and ΔT is the change in temperature causing the linear thermal expansion. The CTE values for the L-PBF samples were found to be between 10.7E and 06 and 12E-06/°C; sample V1 was tested to have a CTE of 10.8E-06/°C and for V2 and V3, CTE was found to be 11.4E-06/°C. These results lie close to the theoretical CTE value of 11E-06/°C for austenite (high temperature) phase in Ni-Ti [51]. The CTE_s were calculated in the high temperature (austenitic) region. No significant correlations were found between the process parameters and CTE. The thermal expansion coefficients generally decrease with an increase in the bond energy. A higher bond energy also results in higher melting point. Therefore, the CTE will be lower in a material that has higher melting point. Since, the compositional variation of L-PBF samples in this study are not considerable, this has not caused any significant change in the CTE.

From the CTE evolution and thermal strain curves shown in Fig. 18, we can see abrupt dips or humps during heating and cooling. These dips or humps indicate a sudden shrinkage or expansion of the material. These characteristic dip/hump indicates solid-state phase transformations as the temperature changes causing the instrument probe that is in contact with the sample, to detect an abrupt contraction or expansion of the sample [52]. The entry and exit tangents (Fig. 18(a)) of these humps in thermal strain curve give an estimation of the corresponding transformation temperatures. Since the machine could not cool the sample below room temperature, the *Mf* temperatures have been excluded. The transition after the start of austenite phase was not clear enough in heating cycle, and therefore only *Ms*, *Rs**, and *As* were focussed in the study. As seen in Fig. 19, the temperatures were close enough to the values found through the DSC curves. *Ms* and *Rs** showed high correlations (r = 0.536 and 0.473 respectively) between the two methods (DSC and dilatometry). There was no significant correlation between the *As* temperatures obtained by the two methods. The difference in *Ms* values obtained through

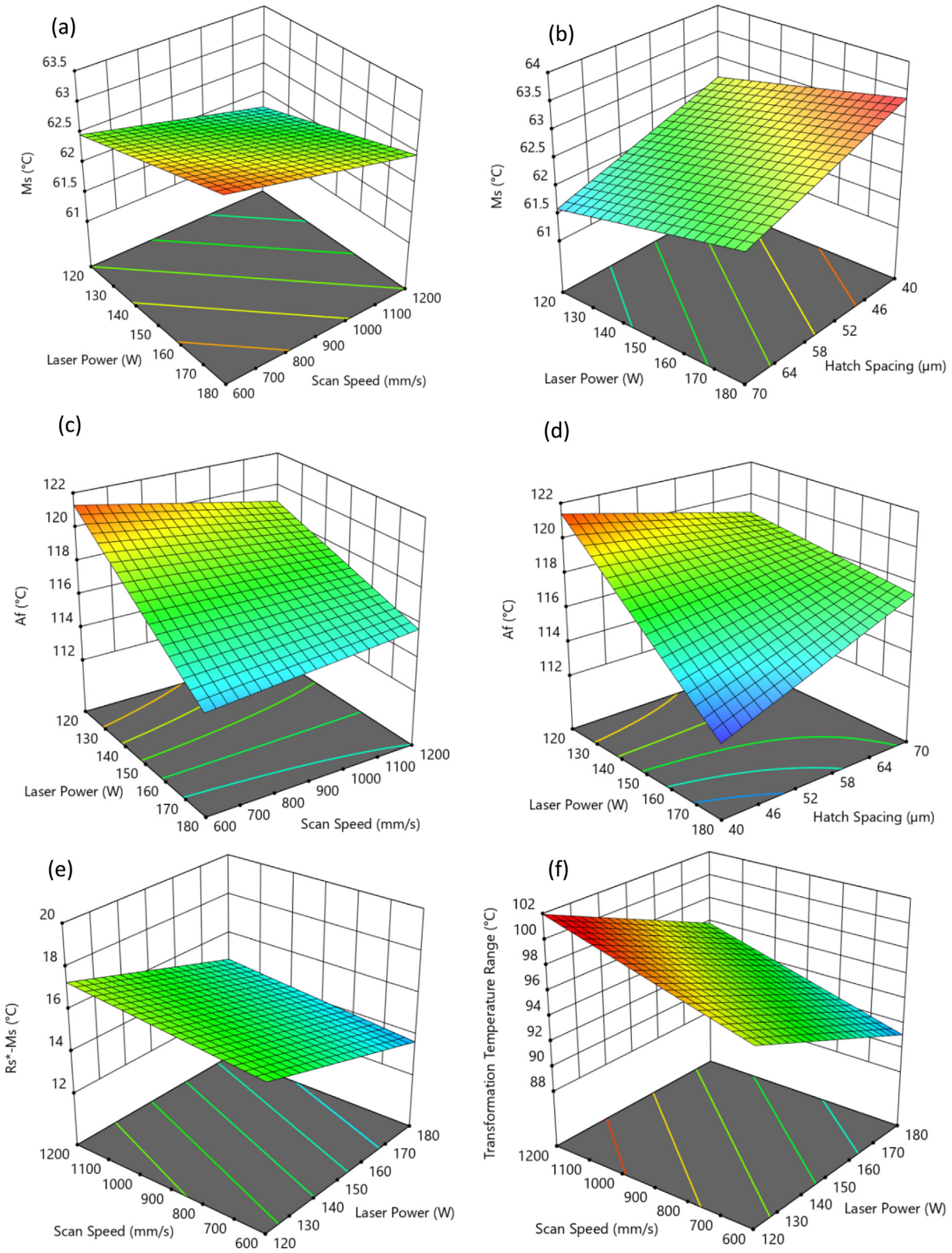

Fig. 16. Response surfaces of laser process parameters on transformation temperatures of vertical samples keeping the third parameter at middle level: martensite start (a, b); austenite finish (c, d); R-phase to martensite transition range (e); Full transformation temperature range (f).

the two methods ranges between 1.4 and 7.8 °C; difference between *Rs** values ranges 0.2–5.5 °C; and for *As* the range was found to be between 0.2 and 15.8 °C. Large variations in CTE will be observed when a phase transformation occurs. To explain the expansion phenomenon in Ni-Ti, both the DSC and dilatometry data can be referred to.

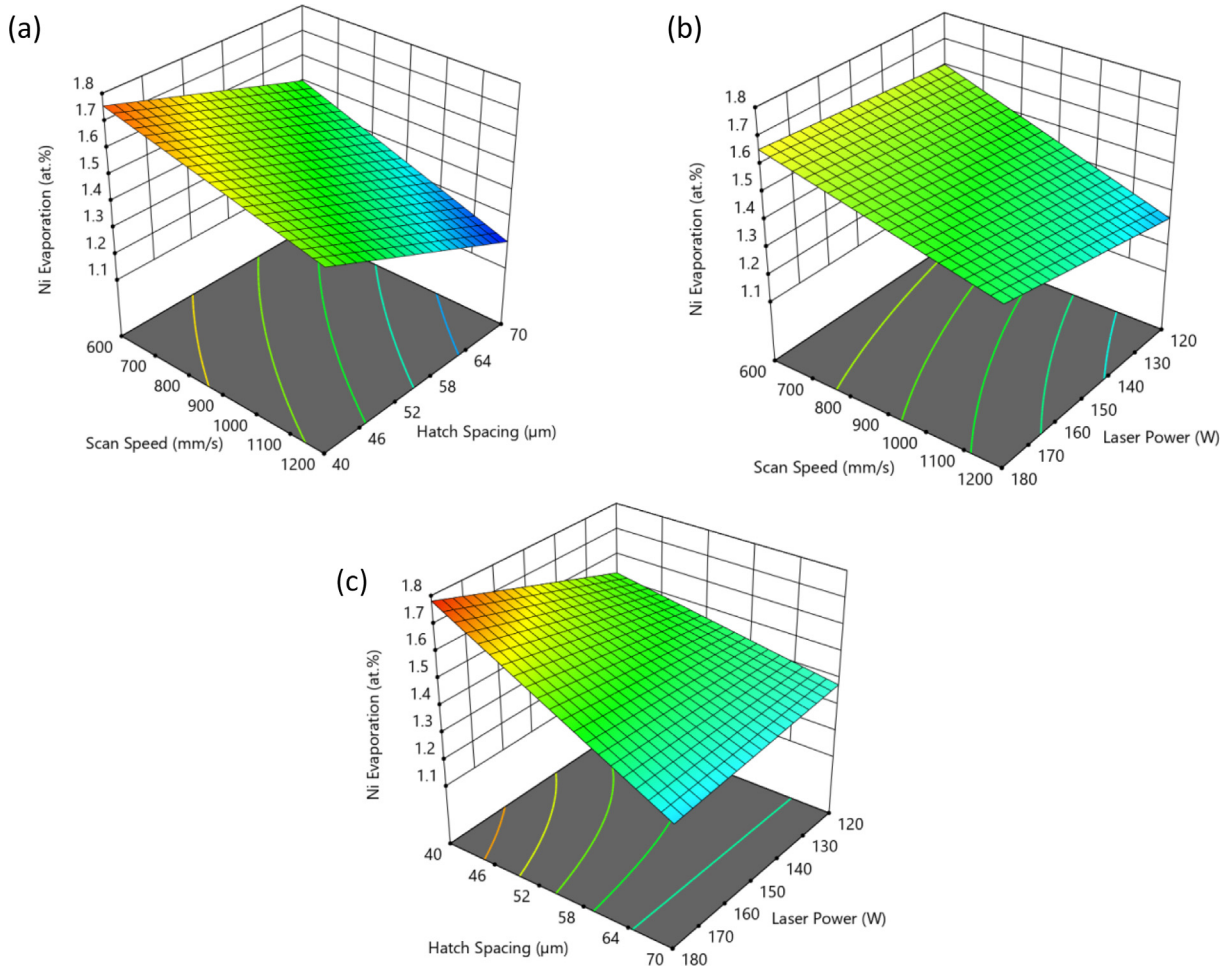

Fig. 17. Response surfaces for Ni evaporation resulting from the L-PBF process showing the effects of (a) scan speed and hatch spacing, (b) scan speed and laser power, and (c) hatch spacing and laser power.

Due to the monoclinic structure of the martensite phase, it is possible for the martensite during transformation to form 24 different variants [53,54], and select a crystallographic equivalent variant as it transforms into austenite phase. Since, there is a fractional presence of R-phase in sample V2 as observed in DSC and XRD analysis, when the Ni-Ti is heated crossing *Ms* temperature, the crystal lattice tends to conform to the phase variant that has lower free energy. Martensite phase has been found to have lowest energy, while the R-phase has an intermediate, and austenite having the highest free energies as shown in Fig. 20. It should be noted that the difference between the free energies of R-phase and austenite is not significant, and the lattice always prefers to choose the phase that has a lower free energy state for stability.

The dips and humps in Fig. 18(b) can be explained based on the transformation between each phase, which often results in an expansion or contraction depending on the lattice parameters of the crystal structures. The monoclinic B19′ martensite lattice parameters are a = 2.877 Å, b = 4.686 Å and c = 4.099 Å, while the austenite B2 (BCC) structure has a shorter lattice a = 3.014 Å. Therefore, an *M* to *A* transformation results in a change in the lattice parameters: a increases by 7%, while b and c decreases by 8.8% and 1.6%. However, the overall unit-cell volume differs by only 0.4% [55]. In the case of rhombohedral R-phase, lattice parameters are defined in terms of hexagonal lattice index having a = 7.358 Å and c = 5.2855 Å. A rhombohedral unit cell is a skewed version of BCC austenite elongated by 0.94% in the [1 1 1] direction [56]. Therefore, a transformation from R^* to *A* is likely to cause contraction.

As observed in Fig. 18(b), the CTE is initially constant (≈ 8E-06/°C, close to the theoretical CTE of martensite phase [51]) when heated from room temperature. Once the temperature crosses *Ms*, the martensite shifts to a lower energy variant while transforming to an R-phase variant. This can result in a dip in the CTE. This dip is further deepened to a few negative CTE values, which indicates a contraction as temperature rises. Depending on the homogeneity of the material, austenite and R-phase can coexist with clear boundary between them [58]. Owing to this possibility, some of the martensite may start to transform to austenite directly instead of transitioning through an R-phase. This causes a negative CTE as the lattice contracts with an increase in temperature. Moreover, the R^* in sample V2 is an unstable variant, and exists as a shoulder on the austenitic transformation. This points towards an inhomogeneity in the bulk phase compositions.

When the material is further heated to above R^*, R-phase starts to form indicating a sharp surge in CTE values due to an elongation in the lattice. Once the temperature is around *As*, the CTE values start to gradually level off and decrease (R^* to *A* lattice contraction) until *Af* is crossed, after which the curve gradually stabilises to austenitic CTE value ≈ 11.4E-06/°C. Both martensitic and austenitic CTE values were found to be very close to the theoretical values. While cooling, due to the incapability of the instrument, the cooling rate could not be maintained. This resulted in the cooling

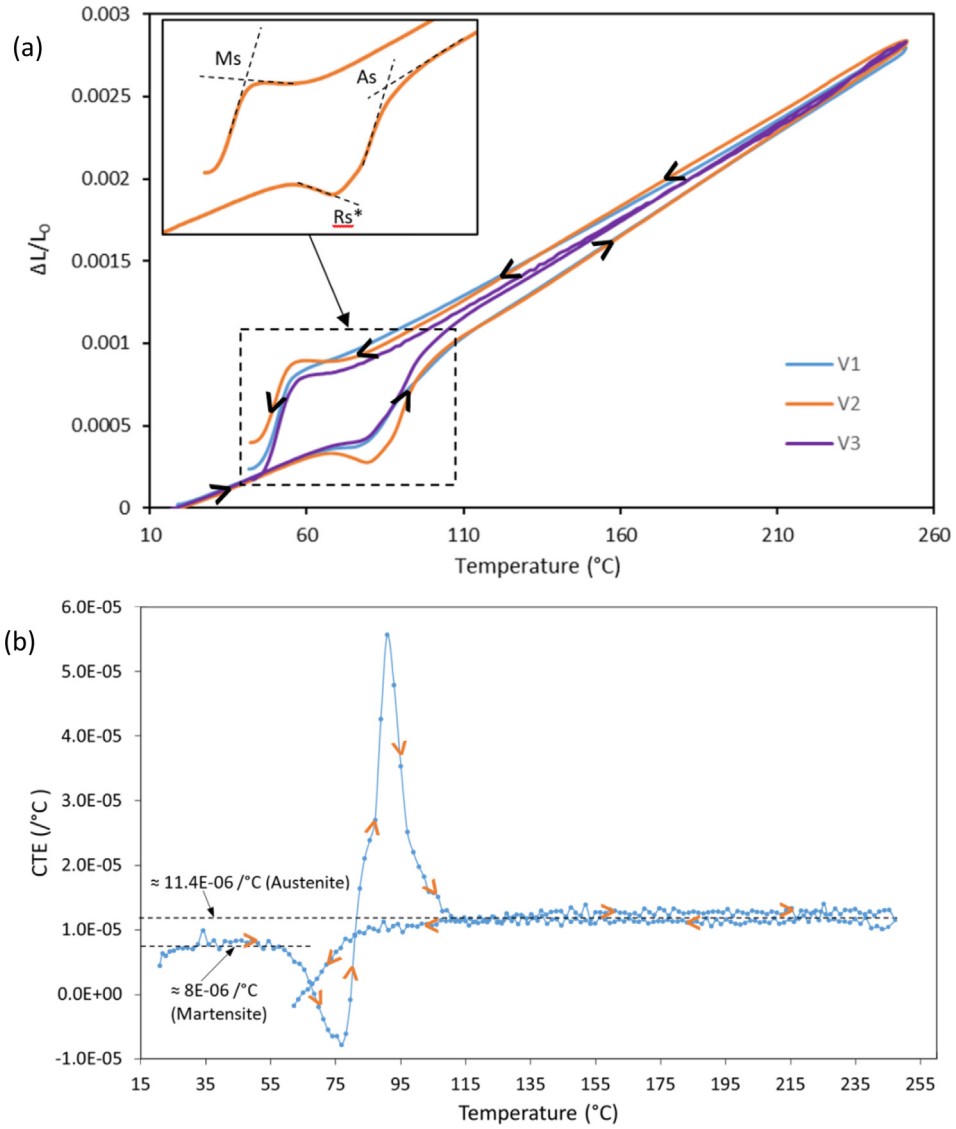

Fig. 18. Plots of the (a) thermal strain curve for samples V1, V2 and V3 showing austenite and martensite phase transformations; and the (b) evolution of CTE with temperature for sample V2.

rate decreasing rapidly as natural cooling started to take over from around 70 °C and below. Due to this anomaly, the CTE evolution of the sample could not be properly understood as it highly depends on the cooling rate. However, this would not affect the determination of the *Ms* from the thermal strain curve, as the peak is dependent on the temperature changes. CTE evolution curve was therefore plotted only till 60 °C for the cooling cycle, to see the trend of the curve. Even though the actual mechanics are not understood, it can be seen that there has been a dip going to the negative CTE region. This indicates a possible lattice transformation from austenite to a martensite, owing to an elongation of the unit cell.

4. Conclusions

As-fabricated Ni-Ti samples were 3D printed using the L-PBF (SLM) technique, and the effect of process parameters on the part density, material composition and phase transformation temperatures were analysed. To examine the relative part densities, the effect of build orientations (horizontal and vertical) were also considered. Variation in densities among the L-PBF samples were linked to the thermograph findings, and certain process-related defects. The laser energy input caused Ni evaporation which results in higher transformation temperatures than that of the raw material used. The transformation behaviour was further investigated in detail based on the DSC graphs. The endothermic and exothermic enthalpy changes associated with phase transformations were also compared and investigated to elucidate the extent of transformations. The thermal expansion characteristics for the printed samples were also studied, via dilatometry. The generated results helped in exploring the underlying mechanics of linear expansion in Ni-Ti, and comparing the TTs to that produced via DSC analysis. All significant correlations between the input process parameters and the characterisation results were presented in the form of response surfaces and actual equations. The following conclusions summarise the important findings from this work:

1. The relative densities of samples printed horizontally showed higher variations between 93.4% and 98.5%, while vertically printed samples showed only small variations resulting in densities of 97.2% to 97.9%. For the current parameter levels, the *RD* of vertical samples presented a linear and two-factor interactive

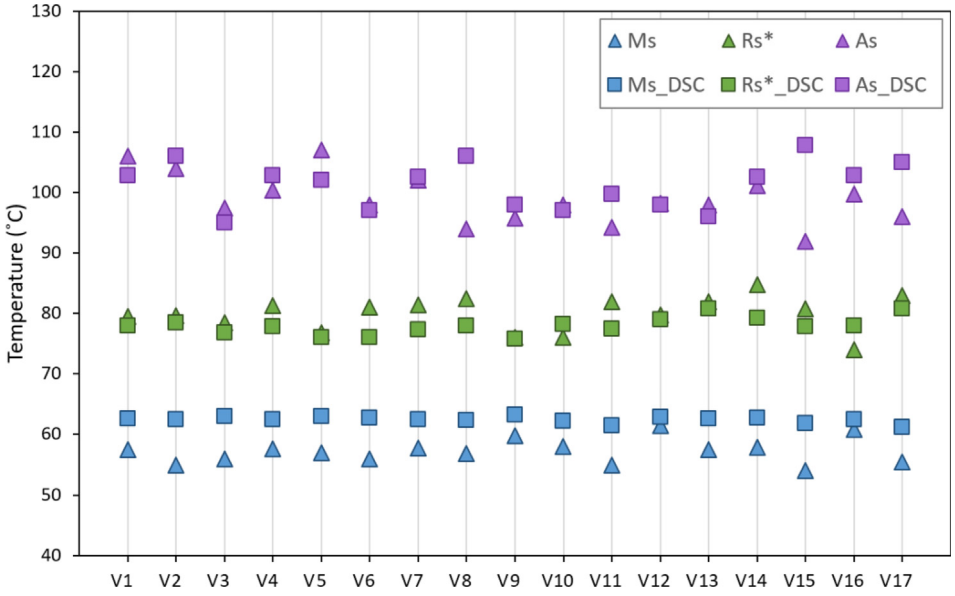

Fig. 19. Transformation temperatures (martensite start, *Ms*; R-phase start, *Rs**; austenite start, *As*) from dilatometry data compared with the ones obtained from DSC analysis.

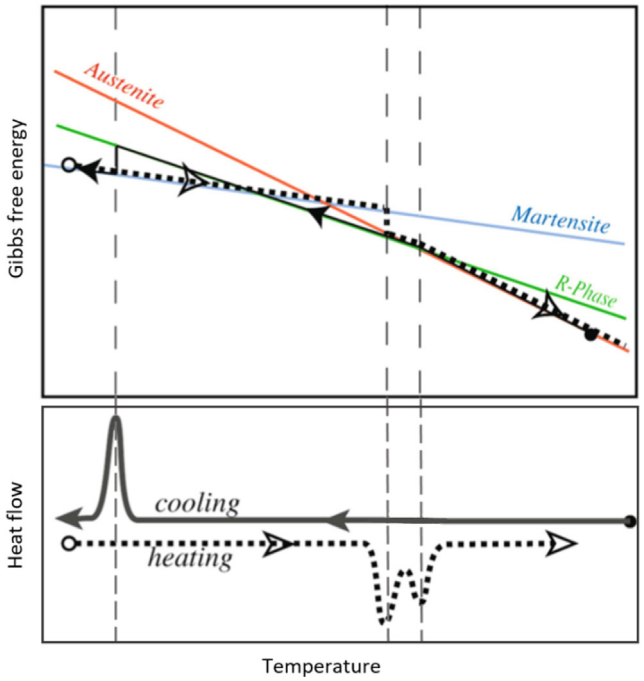

Fig. 20. Illustration of Gibbs free energy of martensite, R-phase and austenite phases at different temperatures, compared with the DSC curve similar to the L-PBF samples in this work; dotted line represents heating cycle; figure reproduced from Deurig and Bhattacharya (2015) [57].

relation, while the *RD* of horizontal samples showed an additional quadratic relation also, with the laser process parameters. For the horizontal samples, an inverse effect between *RD* and *VED* was also found; highest impact was found to be from the scan speed. Low densities were found to be linked to porosity defects that are cause by trapped/escaped gas voids, keyhole formations, and defective powder particles. The structures also contained microcracks formed from residual thermal stresses.

2. The difference in densities of the samples printed vertically and horizontally were linked to the intralayer temperature differentials. Higher difference in TD_{avg} causes larger differences in densities of samples printed in either orientation. The vertical samples were found to have a lower TD_{avg}, which resulted in a higher average density and the lower density variability compared to the horizontally printed samples.
3. In general, L-PBF samples were found to contain an unstable overlapped R-phase with the austenite phase; the finding was corroborated in XRD analysis also. Compared to the raw powders, the L-PBF samples showed higher TTs associated with the reduction in Ni content. The *Mf* temperatures elevated by 1.2 to 9.0 °C. *Ms* temperatures increased by 11.8 to 13.9 °C; showed a linear relation to the process parameters. *Rs** elevated by about 20 to 25 °C, and *Rf**/*As* by 7.0 to 19.8 °C. *Af* increased by 5.0 to 13.9 °C, and showed a linear and two-factor interactive relation to the process parameters. Both *RMTR* and *TTR* showed linear relations to the laser parameters.
4. The transition enthalpies for *A* to *M* and *M* to *A* transitions differed considerably, giving rise to lower transition enthalpy ratios (0.72 to 0.83) whereas the enthalpy ratios for raw powders were quite high (0.97); this was related to the extent of material that has undergone phase transformations.
5. The Ni content was found to reduce by 1.2 to 1.8 at.% under the parameter levels used in this work. A linear and two-factor interactive relation was found to exist between the Ni evaporation and the laser parameters. *VED* exhibited a high direct correlation (>85%) with the Ni evaporation. Scan speed and hatch spacing were found to have a negative correlation to this occurrence. Considering the above findings, we can conclude that the feedstock (pre L-PBF) composition combined with the potential of L-PBF process parameters to cause Ni evaporation (which alters the TTs) can be exploited to process Ni-Ti for specific applications. For instance, for heat pump applications, TTs in the range of 70 to 100 °C is optimal for the operation conditions, whereas, lower TTs in the range of −20 to 10 °C will be optimal for superelastic applications.
6. The linear *CTE* s for L-PBF samples were found to vary between 10.7E-06 and 12E-06/°C under the austenitic region, and be approx. 8E-06/°C for the martensitic region, in close agreement to the theoretical values. The transformation temperatures found via dilatometry and DSC were also in good agreement.

The above findings were for the current selection of process parameters and levels. These could differ greatly with respect to the material composition chosen, operation environment, and range of parameters used. For instance, the relationship between *VED* and part density does not clearly explain how density can be controlled, this strongly encourages the need for a new relationship that considers different aspects of the L-PBF process, such as powder material characteristics, laser processing properties and inert-gas flow properties, in more detail. A few of the defects could be avoided prior to the process itself, for instance, a meticulous preparation and recycling of raw powders processed with good morphology and rheology can help to avoid chances of certain internal porosities. Substrate preheating can help to reduce the residual thermal stresses. Indeed typically, the as-fabricated samples are preferred to undergo annealing or thermal post-processing in order to relieve thermal stresses, and combat the formation of precipitates and secondary phases that affects the matrix composition and/or the SME characteristics. In future work, it is planned that the resulting physical properties will be examined further.

Declaration of Competing Interest

The authors declare that they have no known competing financial interests or personal relationships that could have appeared to influence the work reported in this paper.

Acknowledgement

This publication has emanated from research supported in part by a grant from Science Foundation Ireland under Grant number 16/RC/3872 and 18/EPSRC-CDT/3584. For the purpose of Open Access, the author has applied a CC BY public copyright licence to any Author Accepted Manuscript version arising from this submission.

References

[1] S. Dadbakhsh, M. Speirs, J. van Humbeeck, J.P. Kruth, Laser additive manufacturing of bulk and porous shape-memory NiTi alloys: from processes to potential biomedical applications, MRS Bull. 41 (2016) 765–774.
[2] M. Bram, A. Ahmad-Khanlou, A. Heckmann, B. Fuchs, H.P. Buchkremer, D. Stöver, Powder metallurgical fabrication processes for NiTi shape memory alloy parts, Mater. Sci. Eng. 337 (1-2) (2002) 254–263.
[3] C.M. Jackson, H.J. Wagner, R.J. Wasilewski, 55 Nitinol—The Alloy with a Memory: Its Physical Metallurgy, Properties, and Applications, NASA SP-5110, NASA: Washington, DC, USA, 1972.
[4] M.H. Elahinia, M. Hashemi, M. Tabesh, S.B. Bhaduri, Manufacturing and processing of NiTi implants: a review, Prog. Mater. Sci. 57 (5) (2012) 911–946.
[5] J.C. Chekotu, R. Groarke, K. O'Toole, D. Brabazon, Advances in selective laser melting of nitinol shape memory alloy part production, Mater. 12 (2019) 809.
[6] S. Saedi, Shape Memory Behavior of Dense and Porous NiTi Alloys Fabricated by Selective Laser Melting, University of Kentucky, Lexington, KT, USA, 2017. Ph.D. Thesis.
[7] M.N. Shayesteh, Toward Patient Specific Long Lasting Metallic Implants For Mandibular Segmental Defects, University of Toledo, USA, 2015. MSc Thesis.
[8] I.V. Shishkovsky, L.T. Volova, M.V. Kuznetsov, Y.G. Morozov, I.P. Parkin, Porous biocompatible implants and tissue scaffolds synthesized by selective laser sintering from Ti and NiTi, J. Mater. Chem. 18 (2008) 1309–1317.
[9] M.T. Andani, N. Shayesteh Moghaddam, C. Haberland, D. Dean, M.J. Miller, M. Elahinia, Metals for bone implants part 1 – powder metallurgy and implant rendering, Acta Biomater. 10 (10) (2014) 4058–4070.
[10] N.S. Moghaddam, R. Skoracki, M. Miller, M. Elahinia, D. Dean, Three dimensional printing of stiffness-tuned, nitinol skeletal fixation hardware with an example of mandibular segmental defect repair, Proc. CIRP 49 (2016) 45–50.
[11] B. O'Brien, M. Bruzzi, Shape memory alloys for use in medicine, in: P. Ducheyne (Ed.), Comprehensive Biomaterials, Elsevier, USA, 2011, pp. 49–72.
[12] D. Stoeckel, A. Pelton, T. Duerig, Self-expanding nitinol stents: material and design considerations, Eur. Radiol. 14 (2004) 292–301.
[13] G. Florian, A.R. Gabor, C.A. Nicolae, A. Rotaru, N. Stănică, N.G. Bîzdoacă, P. Rotaru, Thermomechanical, calorimetric and magnetic properties of a Ni-Ti shape-memory alloy wire, J. Therm. Anal. Calorim. 140 (2) (2020) 527–544.
[14] J.M. Gallardo Fuentes, P. Gümpel, J. Strittmatter, Phase change behavior of nitinol shape memory alloys, Adv. Eng. Mater. 4 (7) (2002) 437–452.
[15] T. Bormann, R. Schumacher, B. Müller, M. Mertmann, M. de Wild, Tailoring selective laser melting process parameters for NiTi implants, J. Mater. Eng. Perform. 21 (12) (2012) 2519–2524.
[16] T. Bormann, M. de Wild, F. Beckmann, B. Muller, Assessing the Morphology of Selective Laser Melted NiTi Scaffolds for a Three-Dimensional Quantification of the One-Way Shape Memory Effect, Proceedings of the SPIE Conference, San Diego, CA, USA, 2013.
[17] S. Saedi, A.S. Turabi, M.T. Andani, N.S. Moghaddam, M.H. Elahinia, H.E. Karaca, Texture, aging, andsuperelasticity of selective laser melting fabricated Ni-rich NiTi alloys, Mater. Sci. Eng. 686 (2017) 1–10.
[18] M. Speirs, X. Wang, S. Van Baelen, A. Ahadi, S. Dadbakhsh, J.-P. Kruth, J. Van Humbeeck, On the transformation behavior of NiTi shape-memory alloy produced by SLM, Shape Mem. Superelast. 2 (4) (2016) 310–316.
[19] M.H. Elahinia, Shape Memory Alloy Actuators: Design, Fabrication and Experimental Evaluation, John Wiley & Sons, 2016.
[20] M.A. Obeidi, S.M. Uı Mhurchadha, R. Raghavendra, A. Conway, C. Souto, D. Tormey, I. Ul Ahad, D. Brabazon, Comparison of the porosity and mechanical performance of 316L stainless steel manufactured on different laser powder bed fusion metal additive manufacturing machines, J. Mater. Res. Technol. 13 (2021) 2361–2374.
[21] T. Bormann, B. Muller, M. Schinhammer, A. Kessler, P. Thalmann, M. de Wild, Microstructure of selective laser melted nickel-titanium, Mater. Charact. 94 (2014) 189–202.
[22] S. Dadbakhsh, B. Vrancken, J.P. Kruth, J. Luyten, J. van Humbeeck, Texture and anisotropy in selective laser melting of NiTi alloy, Mater. Sci. Eng. 650 (2016) 225–232.
[23] B.o. Song, X. Zhao, S. Li, C. Han, Q. Wei, S. Wen, J. Liu, Y. Shi, Differences in microstructure and properties between selective laser melting and traditional manufacturing for fabrication of metal parts: a review, Front, Mech. Eng. 10 (2) (2015) 111–125.
[24] S. Dadbakhsh, M. Speirs, J.-P. Kruth, J. Schrooten, J. Luyten, J. Van Humbeeck, Effect of SLM parameters on transformation temperatures of shape memory nickel titanium parts, Adv. Eng. Mater. 16 (9) (2014) 1140–1146.
[25] M.A. Obeidi, M. Monu, C. Hughes, D. Bourke, M. Nur Dogu, J. Francis, M. Zhang, I. Ul Ahad, D. Brabazon, Laser beam powder bed fusion of nitinol shape memory alloy (SMA), J. Mater. Res. Technol. 14 (2021) 2554–2570.
[26] P. Stoll, A. Spierings, K. Wegener, SLM processing of elementally blended NiTi shape memory alloy, Proc. CIRP. 95 (2020) 121–126.
[27] N. Shayesteh Moghaddam, S. Saedi, A. Amerinatanzi, A. Hinojos, A. Ramazani, J. Kundin, M.J. Mills, H. Karaca, M. Elahinia, Achieving superelasticity in additively manufactured NiTi in compression without post-process heat treatment, Sci. Rep. 9 (1) (2019).
[28] P. Bayati, K. Safaei, M. Nematollahi, A. Jahadakbar, A. Yadollahi, M. Mahtabi, M. Elahinia, Toward understanding the effect of remelting on the additively manufactured NiTi, Int. J. Adv. Manuf. Technol. 112 (1-2) (2021) 347–360.
[29] J. Ma, B. Franco, G. Tapia, K. Karayagiz, L. Johnson, J. Liu, R. Arróyave, I. Karaman, A. Elwany, Spatial control of functional response in 4d-printed active metallic structures, Sci. Rep. 7 (2017) 46707.
[30] S. Saedi, M.N. Shayesteh, A. Amerinatanzi, M. Elahinia, H.E. Karaca, On the effects of selective laser melting process parameters on microstructure and thermomechanical response of Ni-rich NiTi, Acta Mater. 144 (2018) 552–560.
[31] J. Walker, M. Elahinia, C. Haberland, An Investigation of Process Parameters on Selective Laser Melting of Nitinol, ASME 2013 Conference on Smart Materials, Adaptive Structures and Intelligent Systems, 2013.
[32] H. Meier, C. Haberland, J. Frenzel, Structural and Functional Properties of NiTi Shape Memory Alloys Produced by Selective Laser Melting, Innovative Developments in Virtual and Physical Prototyping, Proceedings of the 5th International Conference on Advanced Research in Virtual and Rapid Prototyping, 2012.
[33] C. Haberland, M. Elahinia, J. Walker, H. Meier, J. Frenzel, On the development of high quality NiTi shape memory and pseudoelastic parts by additive manufacturing, Smart Mater. Struct. 23 (2014) 104002.
[34] S. Das, Physical aspects of process control in selective laser sintering of metals, Adv. Eng. Mater. 5 (10) (2003) 701–711.
[35] A. Sola, A. Nouri, Microstructural porosity in additive manufacturing: The formation and detection of pores in metal parts fabricated by powder bed fusion, J. Adv. Manuf. Process. 1 (2019) 10021, https://doi.org/10.1002/amp2.10021.
[36] X. Zhao, D. Gu, C. Ma, L. Xi, H. Zhang, Microstructure characteristics and its formation mechanism of selective laser melting SiC reinforced Al-based composites, Vacuum 160 (2019) 189–196.
[37] S.V. Chernyshikhin, D.G. Firsov, I.V. Shishkovsky, Selective Laser Melting of Pre-Alloyed NiTi Powder: Single-Track Study and FE Modeling with Heat Source Calibration, Mater. 14 (2021) 7486.
[38] J.Y. Lee, S.H. Ko, D.F. Farson, C.D. Yoo, Mechanism of keyhole formation and stability in stationary laser welding, J. Phys. D: Appl. Phys. 35 (2002) 1570–1576.
[39] X. He, J.T. Norris, P.W. Fuerschbach, T. Debroy, Liquid metal expulsion during laser spot welding of 304 stainless steel, J. Phys. D: Appl. Phys. 39 (2006) 525–534.
[40] J.N. Zhu, E. Borisov, X. Liang, E. Farber, M.J.M. Hermans, V.A. Popovich, Predictive analytical modelling and experimental validation of processing maps in additive manufacturing of nitinol alloys, Addit. Manuf. 38 (2021) 101802.

[41] K.A. Mumtaz, N. Hopkinson, Selective laser melting of thin wall parts using pulse shaping, J. Mater. Process. Technol. 210 (2) (2010) 279–287.
[42] Y. Yang, Y. Huang, W. Wu, One-Step Shaping of NiTi Biomaterial by Selective Laser Melting, Photonics Asia, International Society for Optics and Photonics, Bellingham, WA, USA, 2007.
[43] R.F. Hamilton, T.A. Palmer, B.A. Bimber, Spatial characterization of the thermal-induced phase transformation throughout as-deposited additive manufactured NiTi bulk builds, Scr. Mater. 101 (2015) 56–59.
[44] J. Walker, M.T. Andani, C. Haberland, M. Elahinia, Additive Manufacturing of Nitinol Shape Memory Alloys to Overcome Challenges in Conventional Nitinol Fabrication, Proceedings of the ASME 2014 International Mechanical Engineering Congress and Exposition, Montreal, Quebec, Canada, 2014.
[45] Memry SAES Group Corporation, Introduction to Nitinol. https://www.memry.com/intro-to-nitinol/, 2017 (accessed 30 July 2021).
[46] K.M. Horvay, C.T. Schade, Development of Nitinol Alloys for Additive Manufacturing, Materials Science and Technology (MS&T18), Columbus, Ohio, USA, 2018.
[47] A. Chmielewska, B. Wysocki, J. Buhagiar, B. Michalski, B. Adamczyk-Cieślak, M. Gloc, W. Święszkowski, In situ alloying of NiTi: Influence of laser powder bed fusion (LBPF) scanning strategy on chemical composition, Mater. Today Commun. 30 (2022), 103007.
[48] J.-N. Zhu, E. Borisov, X. Liang, R. Huizenga, A. Popovich, V. Bliznuk, R. Petrov, M. Hermans, V. Popovich, Controlling microstructure evolution and phase transformation behavior in additive manufacturing of nitinol shape memory alloys by tuning hatch distance, J. Mater. Sci. 57 (10) (2022) 6066–6084.
[49] S.F. Madlul, A.N. Abd, H.M. Miklif, Phase investigation of nitinol sma according to melting method, NeuroQuantology 18 (2020) 73–76.
[50] I. Müller, S. Seelecke, Thermodynamic aspects of shape memory alloys, Math. Comput. Model. 34 (12-13) (2001) 1307–1355.
[51] W.B. Cross, A.H. Kariotis, F.J. Stimler, Nitinol Charaterization Study, NASA CR-1433, Ohio, USA, 1969.
[52] G. Florian, A.R. Gabor, C.A. Nicolae, A. Rotaru, C.A. Marinescu, G. Iacobescu, N. Stănică, S. Degeratu, O. Gîngu, P. Rotaru, Physical and thermophysical properties of a commercial Ni–Ti shape memory alloy strip, J. Therm. Anal. Calorim. 138 (3) (2019) 2103–2122.
[53] F. Auricchio, R.L. Taylor, J. Lubliner, Shape memory alloys: macromodelling and numerical simulations of the superelastic behavior, Comput. Meth. Appl. Mech. Eng. 146 (3-4) (1997) 281–312.
[54] A. Paiva, M.A. Savi, An overview of constitutive models for shape memory alloys, Math. Prob. Eng. 2006 (2006) 1–30.
[55] K. Parlinski, M. Parlinska-Wojtan, Lattice dynamics of NiTi austenite, martensite, and R phase, Phys. Rev. B 66 (2002) 064307.
[56] M. Kubenova, Processing and Martensitic Transformations of NiTi-Based Alloys, BRNO University of Technology, Czech Republic, 2014. PhD Thesis.
[57] T.W. Duerig, K. Bhattacharya, The influence of the r-phase on the superelastic behavior of NiTi, Shap. Mem. Superelast. 1 (2) (2015) 153–161.
[58] T. Tamiya, D. Shindo, Y. Murakami, Y. Bando, K. Otsuka, In-situ observations of r-phase transformation in a Ti50Ni48Fe2 alloy by electron microscopy, Mater. Trans. 39 (1998) 714–723.